

Copyright

by

Michael Phillip Merrell

2012

**The Thesis Committee for Michael Phillip Merrell
Certifies that this is the approved version of the following thesis:**

Pressure and Stress at Mad Dog Field, Gulf of Mexico

**APPROVED BY
SUPERVISING COMMITTEE:**

Supervisor:

Peter B. Flemings

Michael R. Hudec

Marc Hesse

Chris Walker

Pressure and Stress at Mad Dog Field, Gulf of Mexico

by

Michael Phillip Merrell, B.S.Geo.

Thesis

Presented to the Faculty of the Graduate School of

The University of Texas at Austin

in Partial Fulfillment

of the Requirements

for the Degree of

Masters of Science in Geological Sciences

The University of Texas at Austin

December 2012

Acknowledgements

I would like to thank my parents for their love and support throughout graduate school. Most of all I would I like to think my wife for her support, love, and patience while pursuing a master degree.

I am truly grateful to have such great officemates Andrew, Will, and Baiyuan, for their help and guidance while pursing my degree at the University of Texas. I would like to especially like to thank Andrew for all his help with Landmark, GMT, Matlab, and any other software that we had the opportunity to learn. I am grateful for knowing and learning from two posts docs Maria and Gang in our UT Geofluids Consortium. I also have the great privilege of getting to know and learning from Julia, Yao, Derek, Michael C., and Peter P. I would also like to thank Tessa Green for all your help and getting me onto Peter's extremely busy schedule and organizing our annual meetings and travel arrangements.

Thanks to my advisor, Dr. Peter Flemings, for supervising my thesis project. I am truly blessed and fortunate to have been advised by such an intelligent and passionate scientist. Peter has truly pushed me as a scientist further than I can imagine. I still remember my first awful presentation to the Geofluids lab group the first semester and how I have progressed through these past two years as a more confident presenter through Peter's hard work and help. Thank you for believing in me and pushing me to be a better scientist, presenter, and writer. I would also like to thank my co-advisor, Mike Hudec for all his help and allowing me to have access to the seismic data at BEG.

Lastly, I am thankful for the financial support from the UT/MIT Geofluids Consortium and the Statoil Fellowship.

Abstract

Pressure and Stress at Mad Dog Field, Gulf of Mexico

Michael Phillip Merrell, M.S.Geo.Sci.

The University of Texas at Austin, 2012

Supervisor: Peter B. Flemings

Hydrocarbon exploration involves drilling into or near salt deposits in the Gulf of Mexico, Brazil, Egypt, and the Middle East. Drilling these systems has proven to be quite dangerous, challenging, and expensive due to the pressure and stress perturbations that exist around the salt. My study focuses on characterizing the pressure and stress distribution at the Mad Dog field, which is a large oil field below an allochthonous salt body in the deepwater Gulf of Mexico. The Mad Dog field lies beneath the Sigsbee Escarpment, which represents the surface and seaward-most indicator of a mobile salt in Green Canyon blocks 781, 782, 825, and 826, 190 miles southwest of New Orleans in 4,500-6,500 feet of water. I characterize the pressure distribution within the Lower Miocene sandstone reservoir which has produced over 100 million barrels to date. I map the reservoir horizon using 3D seismic data and that the reservoir is a complex regional anticlinal structure that is separated by numerous normal faults that cause it to be segmented into compartments. The in-situ pore pressures show that the compartments are not in pressure communication across the field and that multiple aquifer phase pressures are present.

The in-situ pore pressure measurements are used to characterize the pressure distribution in the Miocene sediments below the salt body and in front of the mobile salt body. These measurements show that between the upper Miocene to middle Miocene there is an absolute pressure decrease and between the middle to lower Miocene there is a large pressure increase. This pressure distribution is seen both within the Miocene sediments below salt and in front of salt. A porosity and effective stress relationship from shallow Pleistocene sediments was developed to predict the pressure behavior observed within the Miocene and compare the predicted pressure with in-situ pore pressure measurements. The mudstone pressure prediction overestimates the in-situ sand pore pressure. The mudstones bounding regional sandstone have a constant porosity throughout the field, suggesting that the vertical effective stress is constant. These observations can be used to estimate the mudstone pore pressure in a new well location. If the vertical effective stress in an offset well is known and given knowledge of the total vertical stress in the new well location, the mudstone pore pressure can be estimated.

Table of Contents

List of Tables	ix
List of Figures	x
Chapter 1: Introduction	1
Chapter 2: Reservoir Fluid and Pressure Distribution at Mad Dog, GOM.....	4
Abstract	4
2.1 Introduction	5
2.2 Field overview and location	6
2.3 Mad Dog structure	8
2.4 Fluid distribution and reservoir pressure	9
2.4.1 Static gradients within individual wells	9
2.4.2 Integrating pressure and log data for hydrocarbon distribution.	11
2.5 Discussion	15
2.6 Conclusion	17
2.7 Figures.....	18
2.8 Tables	28
Chapter 3: Subsalt Pressure Prediction in the Miocene Mad Dog Field, Gulf of Mexico	30
Abstract	30
3.1 Introduction	31
3.2 Overview of the Mad Dog field	32
3.3 Pore pressures at Mad Dog	33
3.3.1 Approach	33
3.3.2 Mad Dog	34
3.4 Relationship between mudstone porosity and vertical effective stress at Mad Dog.....	37
3.4.1 Development of a predictive relationship	37
3.5 Mudstone pressure across Mad Dog	40

3.6 Discussion	43
3.7 Conclusions	48
3.8 Figures.....	50
3.9 Tables	64
Appendix A: Estimation of Total Vertical Stress	69
A.1 Figures.....	71
Appendix B: Methodology for Petrophysical Analysis	73
B.1 Figures.....	75
Appendix C: Pore Pressure Prediction through Velocity	76
C.1 Development of a predictive relationship	76
C.2 Figures	79
Appendix D: Shallow Pore Pressure Data	82
D.1 Figures.....	84
Appendix E: Depth below Seafloor versus Excess Pressure (u^*).....	87
E.1 Figures	88
E.2 Tables	89
Bibliography	90

List of Tables

Table 2.1: Summary table of the pore pressure gradients and densities in the lower Miocene sandstone across the field	28
Table 2.2: Summary table of the pore pressure gradients, fluid contacts, and pressures at the fluid contacts between the fault blocks in the DD sandstone	29
Table 2.3: Summary table of the pore pressure gradients, fluid contacts, and pressures at the fluid contacts between the fault blocks in the EE/FF sandstone	29
Table 3.1: Nomenclature	64
Table 3.2: Sandstone depth below sea-level, depth below seafloor, minimum and maximum excess pressure (u^*), and average excess pressures (u^*) values	65
Table 3.3: Compressibility and reference porosity for Mad Dog and other regions	66
Table 3.4: Mudstone depths, porosity, velocity, and vertical effective stress	67
Table 3.5: Regression parameters ($u^* = a + b(\sigma_v - u_h)$) through the mudstone pressures at Mad Dog	68
Table E.1: Regression parameters ($u^* = a + b(\sigma_v - u_h)$) through the mudstone pressures at Mad Dog using depth	89

List of Figures

Figure 2.1: Location and base map of the Mad Dog field, Gulf of Mexico....	18
Figure 2.2: Regional seismic line across the Mad Dog structure.....	19
Figure 2.3: Structure map of the lower Miocene sandstone	20
Figure 2.4: Schematic diagram showing the technique to characterize reservoir connectivity throughout the field.....	21
Figure 2.5: Type log of the lower Miocene reservoir sands at Mad Dog field from well 782-1	22
Figure 2.6: Type log of the lower Miocene reservoir sands at Mad Dog field from well 783-1	23
Figure 2.7: Pore pressure versus depth plot for the DD sandstone	24
Figure 2.8: Structure map of the DD sandstone and the fluid distribution at Mad Dog.....	25
Figure 2.9: Pore pressure versus depth plot for the EE/FF sandstone	26
Figure 2.10: Structure map of the EE/FF sandstone and the fluid distribution at Mad Dog.....	27
Figure 3.1: Location and base map of the Mad Dog field, Gulf of Mexico....	50
Figure 3.2: Geologic cross section through the Mad Dog field	51
Figure 3.3: Schematic diagram of a sandstone with multiple fluids present and the associated pressures.....	52
Figure 3.4: Pressure versus depth plot of the discovery well 826 #1	53
Figure 3.5: Pressure versus depth plot of the first appraisal well 782 #1	54
Figure 3.6: Total vertical stress gradients and total vertical stress from sea-level and seafloor.....	55

Figure 3.7: Example of relating direct pore pressure in sandstone to the offset mudstone for porosity and vertical effective stress calibration in well 826 #1.....	56
Figure 3.8: Mudstone porosity versus vertical effective stress in well 826 #1	57
Figure 3.9: Pressure versus depth plot of well 783 #1	58
Figure 3.10: Pressure versus depth plot of well 826 #5	59
Figure 3.11: Difference between sandstone and mudstone pressures in the middle and lower Miocene	60
Figure 3.12: Constant mudstone porosity near the N sandstone	61
Figure 3.13: Sandstone and mudstone pressures across the field	62
Figure 3.14: Schematic sandstone and mudstone pressure below salt.....	63
Figure A.1: Bulk densities for wells 826 #1, 782 #1, 783 #1, and 826 #5 used to calculate total vertical stress	71
Figure A.2: Example calculation of the total vertical stress with salt present at Mad Dog from well 782 #1	72
Figure B.1: Picking the mudstone intervals in well 826 #1	75
Figure C.1: Pleistocene mudstone velocity versus vertical effective stress in well 826 #1.....	79
Figure C.2: Pressure versus depth plot of the discovery well 826 #1 using a velocity and vertical effective stress relationship to predict pressure	80
Figure C.3: Pressure versus depth plot of the first appraisal well 782 #1 using a velocity and vertical effective stress relationship to predict pressure	81
Figure D.1: Direct pressure measurements in the N sandstone.....	84

Figure D.2: Direct pressure measurements in the PQRS sandstone	85
Figure D.3: Direct pressure measurements in the V sandstone.....	86
Figure E.1: Sandstone and mudstone pressures across the field (depth below seafloor versus excess pressure).....	88

Chapter 1: Introduction

Significant salt deposits are found in the Gulf of Mexico, offshore west Africa and Brazil, in the southern North Sea, Egypt, and the Middle East (Willson and Fredrich, 2005). The salt deposits are actively drilled into or in close proximity for hydrocarbon exploration.

Drilling through or in close proximity to salt systems has proven to quite dangerous, challenging, and expensive (Rohleder et al., 2003; Sweatman et al., 1999; Whitson and McFadyen, 2001; Willson and Fredrich, 2005). Drilling and cementing subsalt wells challenge operators due to shear zones that occur above and below salt bodies that result in rising drilling cost (Sweatman et al., 1999). Closure of wells while drilling through salt is a common problem due to salt movement causing wellbore deformation or wellbore collapse (Kim, 1988). Drilling within these zones is difficult because of the narrow range between pore pressure and fracture gradients that can result in lost circulation, hole instability, and pressure-kicks (Sweatman et al., 1999).

The primary concern while planning wells is trying to predict the pore pressure and the fracture gradient with depth. The drilling mud weight must be greater than the pore pressure with depth or such scenarios as a blowout or pressure-kick can occur. When the drilling mud weight approaches the fracture gradient with depth the formation will tend to break down causing a loss in circulation as the drilling mud enters the formation.

Predicting the pore pressure and fracture gradient is typically achieved by using velocity information from seismic or well data (Badri et al., 2001; Ebrom et al., 2006; Sayers et al., 2002). The velocity under salt systems is very hard to get therefore pore pressure prediction from velocity is unreliable. The seismic data around salt bodies and

salt sheets fail to obtain accurate velocities because of the large velocity contrast between the high velocity salt and lower velocity sediment (Raymer et al., 2000). The presence of mobile salt results in minibasins between salt diapirs that cause the seismic wavefield to be distorted (Michell et al., 2007). Predicting the pore pressure and fracture gradient in the subsalt sections and directional control problems are documented as the main difficulties with drilling salt systems (Whitson and McFadyen, 2001). There are also stress perturbations that are present due to salt (Bowers, 2007; Fredrich et al., 2003).

My thesis addresses the study of pore pressure and stress in and near salt systems in two ways. I first use traditional methods to track reservoir pore pressure around the Mad Dog structure. Second, I explore in detail prediction of pore pressure in mudrocks and compare these pressures to the measured reservoir pressures.

In chapter 2, I used the wide azimuth seismic data (WAZ) to map the reservoir horizon across the Mad Dog field. The wireline logging data was used to characterize the fluid contacts within the reservoir sandstones. The in-situ pore pressure measurements in the reservoir are used to characterize the pressure compartments that exist with the highly faulted reservoir sandstones. I interpret the data to show that multiple fluid contacts exist at different depths and the water and oil phase pressure are not in pressure communication due to the presence of faults separating the reservoir into different compartments.

Chapter 3 focuses on characterizing the pore pressure signature across the Mad Dog field from in-situ pore pressure measurements. These measurements show that between the upper to middle Miocene there is an absolute pressure decrease and between the middle to lower Miocene there is a large pressure increase. This behavior is seen both in the Miocene sediments that lie below salt and sediments that do not lie below salt.

In chapter 3, I use porosity and effective stress relationships from shallow Pleistocene sediments at Mad Dog to predict the pore pressure signature observed in the Miocene. The results show that the predicted mudstone pore pressure overestimates the in-situ sandstone pore pressure. The first observation is that the sandstone and mudstone are not in pressure equilibrium. The second observation is that the mudstone pore pressures have the same porosity (velocity), thus inferring that the vertical effective stress is constant across the field. The mudstone pore pressures in the Mad Dog field follow the total vertical stress gradient whereas the adjacent sandstone pressures the hydrostatic pressure gradient. Therefore, if the vertical effective stress bounding a regional sandstone is known from an offset well and then given knowledge of the total vertical stress in a new location, the mudstone pressure can be predicted.

Chapter 2: Reservoir Fluid and Pressure Distribution at Mad Dog, GOM

ABSTRACT

In this study of the deepwater, Gulf of Mexico sub-salt Mad Dog field, I utilize seismic, well log, and pressure data to characterize the reservoir compartments. The initial discovery of the field occurred in 1998 and production began in 2005, where production is from the lower Miocene sandstone. The trap at the Mad Dog field is a complex regional anticlinal structure that is segmented by numerous normal faults that act as pressure compartments across the field. Pore pressure measurements in the in the three producing sandstones (DD, EE, FF) shows that the DD and EE/FF sandstones are not in pressure communication due to the presence of a thick mudstone between them. The EE/FF sandstones exhibit two aquifer pressures and both the DD and EE/FF sandstones exhibit two oil phase pressures across the field. The multiple aquifer and oil phase pressure are attributed to the normal faults compartmentalizing the reservoir.

2.1 INTRODUCTION

Overpressured pore fluids are generated in sedimentary basins when the sedimentation rate exceeds the ability of the fluids to freely escape (Seldon and Flemings, 2005). These overpressures drive fluid flow and affect the state of stress, hydrocarbon migration and entrapment (Flemings and Lupa, 2004). Detection of these overpressures with depth is one of the major issues when drilling in hydrocarbon exploration and development. Mapping and understanding overpressure prior to drilling is vital for safe and accurate hydrocarbon exploration (Carcione and Helle, 2002). Failure to estimate overpressure can lead to slow penetration rates that cause drilling cost to increase, and increase the probability of well control events (Mukerji et al., 2002). In exploration and development the pore pressure needs to be known for several reasons, primarily for drilling wells safely and accurately to prevent blowouts, loss of circulation, and collapsed wellbores.

Once a field is producing, pore pressure heterogeneity should be understood in order to determine compartmentalization. The analysis of fluid contacts and pressure data is critical for defining the compartments (Sweet and Sumpter, 2007). The pressure distribution across a field helps delineate accurate reserves for future development.

In this study I focus on the pressure distribution near Mad Dog field in the deepwater northern Gulf of Mexico basin, which is an actively compacting basin where the shallow pore pressures typically are near hydrostatic pressure and deeper reservoirs are overpressured (Harrison and Summa, 1991). I first characterize the reservoir structure using a 3D seismic volume. Using in-situ pressure measurements, I characterize the overpressure distribution. From the well log data the fluid contacts can be determined to understand the fluid distribution within the sandstone reservoir. The structure, pressure,

and fluid contacts are determined in order to characterize how the sandstones are connected across the field.

2.2 FIELD OVERVIEW AND LOCATION

The Mad Dog field lies directly below an allochthonous salt sheet beneath the Sigsbee Escarpment in deepwater Gulf of Mexico. The Mad Dog field is located in Green Canyon (GC) blocks 781, 782, 825, and 826, 190 miles southwest of New Orleans in 4,000 to 7,000 feet (1,219-2,134 meters) of water (**Fig. 2.1**). The field extends across the Sigsbee Escarpment, which represents the surface and seaward-most indicator of the mobile salt in the northern Gulf of Mexico (Gealy, 1955). The shallow sediments above the allochthonous salt present geohazard risks due to the active salt tectonics causing normal faults and overpressures zones to develop (Orange et al., 2003). The field lies within the Atwater Fold Belt, a contractional fold-and-thrust belt (Moore et al., 2001). The field is a faulted, four-way closure, with the structure being a large north-south trending anticline with production predominantly coming from the Lower Miocene sandstones. The estimated gross reserves are up to four billion barrels of oil equivalent (Gismatullin, 2011).

The Mad Dog discovery well was drilled in 1998 and production began in 2005 with production to date at over 100 million barrels. Amoco first picked up the GC826 block from Shell in 1997, while BP and BHP owned block GC782 starting in 1995. The Mad Dog field was originally discovered using 1996 seismic data. The original 3D seismic survey was a narrow-azimuth survey (NAZ) with the streamer cable length approximately 26,250 feet (8,000 meters). The NAZ delivers high quality images in the supra-salt section but low resolution in the subsalt sections. To improve subsalt imaging a 3D wide azimuth survey (WAZ) was shot in 2004. The WAZ survey had a 4-kilometer

(12,123 feet) cross line offset and a 250-meter (820 feet) shot line spacing (Michell et al., 2007). There were eight cables deployed separated by 125 meter (410 feet) and the two vessels each had two air guns that fired every 37.5 meters (123 feet) (Michell et al., 2007). The wide azimuth improved subsalt imaging but the seismic imaging at Mad Dog continues to be challenging because of the shallow salt body and the presence of small minibasins between salt diapirs in the canopy (Michell et al., 2007).

The field is producing mainly from lower Miocene sands that are interpreted to be turbidite sands deposited in a base of slope to abyssal plain setting as primarily amalgamated sheet sands (Dias et al., 2009). These sands are characterized as basin floor sheet sands.

The reservoir at Mad Dog is divided into three dominant oil producing lower Miocene sandstones termed the DD, EE, and FF sands. These sands are continuous over several miles with an average gross thickness from the top of the DD to FF sandstone of 360 feet (110 meters) (Smith et al., 2001). These sands are stratigraphically continuous throughout the field, but partial penetrations are common in well bores in which small faults have been intersected. The DD and EE sandstone are separated by a thick mudstone sequence with an average thickness of 75 feet (23 meters). The EE and FF sandstones are separated by thin (10-40 feet) mudstones, which are in some cases absent.

Miocene sandstones are also being produced throughout the Atwater Fold Belt in southern Green Canyon. Some of the major subsalt fields producing from the Miocene reservoirs include Atlantis, K2, Shenzi, and Neptune. The Miocene sandstones are continuous over large areas and may be hydrodynamically connected throughout southern Green Canyon (Dias et al., 2009).

The Mad Dog Spar is equipped for both production and drilling operations. The original development consisted of four predrilled wells and eight wells drilled after spar

installation. The production capacity is approximately 80,000 barrels per day of oil, 60 million cubic feet per day of natural gas, and 50,000 barrels of water per day. The drilling radius for the rig is approximately 10,000 feet (3,048 meters). In 2008 Hurricane Ike removed the rig from the Spar and a new rig was installed in March 2012.

The discovery well 826 #1 that drilled in 1998. The first appraisal and subsalt well was 782 #1 in 1999. In 2005, well 825 #1 was drilled in the southwest region of the Mad Dog field and in early 2005 the Mad Dog Spar achieved first oil. The western most area of Mad Dog was drilled in 2005 with well 781 #11 and in 2009 the southernmost extent of the field was drilled with well 826 #5. Most recently in 2011 the northern area of Mad Dog was drilled. Drilling the southern and northern extents of the Mad Dog region has nearly doubled the estimate of Mad Dog reserves (Gismatullin, 2011).

2.3 MAD DOG STRUCTURE

Using the 3D wide azimuth seismic data, the structure of the reservoir can be determined across the field. Poor seismic imaging below the allochthonous salt body makes the lower Miocene reflector difficult to map across the field (**Fig. 2.2**). The lower Miocene interval from the well data was tied to a zero phase reflector across the field.

Below the allochthonous salt there are several normal faults that developed during the Miocene. Many of these faults have small throws, and are difficult to map on seismic data, except for the southeast part of the field which lies outboard of the Sigsbee salt canopy and is easier to interpret. A cross section through the field shows that there are two major normal faults that lie directly below the allochthonous salt body and these are termed the east and west faults, respectively (**Fig. 2.2**). These normal faults trend north-south and deform the top of the regional anticlinal structure. The lower Miocene structure (**Fig. 2.3**) was mapped using the WAZ survey and the fault polygons were provided by

BP. There are several smaller normal faults splay off the two main east and west faults, most of which trend radially to the fold. In the southeast area of the field the normal faults trend predominantly northwest, whereas in the southwest area faults trend northeast

Based on the normal faults around the field and fluid contacts that will be discussed later, the field is divided into different fault blocks. These fault blocks include the northeast, east, south, southwest ridge, and west fault blocks. These fault blocks will be discussed throughout this chapter regarding the pressure communication throughout the lower Miocene sandstones. These various fault blocks and the normal faults that define the blocks are shown in **Fig. 2.3**.

2.4 FLUID DISTRIBUTION AND RESERVOIR PRESSURE

2.4.1 Static gradients within individual wells

The reservoir within the Mad Dog field is compartmentalized by numerous normal faults. In order to understand how these faults act as pressure barriers that divide the reservoir the direct pressure measurements and fluid contacts will be characterized. A key assumption in understanding pressure communication is that the field is in a static state of equilibrium. If the field is in static equilibrium then, if the fluid phase and density is known, the pressure can be extrapolated vertically. Another assumption is that the water and hydrocarbon phase pressures are equal at the fluid contact. Therefore, extrapolating the hydrocarbon phase down a static gradient from in-situ pore pressure measurements to a known fluid contact can provide the in-situ pore pressure at the fluid contact. The difference between the water and oil phase pressures is referred to as capillary pressure. The overlying cap rock has a capillary entry pressure that must be greater than the capillary pressure if the cap rock acts as a seal. A schematic diagram of the technique used to determine how the reservoir connectivity is shown in **Fig. 2.4**.

From the direct pore pressure measurements the gradients within the reservoir DD, EE, and FF sandstones are characterized across the field. By taking a linear regression through the direct pore pressure measurements the gradient and density of the fluid pressures can be determined. In order to accurately characterize the in-situ pore pressure only the virgin pressure wells are used. This is done because the wells that are post-production may record the depleted pore pressure.

The 1st appraisal and subsalt well 782 #1 penetrated the DD, EE, and FF sandstones within the lower Miocene interval. The three sandstones are oil charged based on the resistivity log, thus the direct pore pressure measurements record the oil phase pressure (**Figure 2.5**). Initial observations of the direct pore pressure measurements within the three sands show that the EE and FF sandstones line up on a single hydrocarbon gradient, while the DD sandstone lines up on its own hydrocarbon gradient. The pressure gradient within the DD sandstone is 0.371 psi/ft (8.392 MPa/km) or 0.856 g/cc and within the EE/FF sandstone 0.368 psi/ft (8.324 MPa/km) or 0.849 g/cc

Well 783 #1 just to the northeast of well 782 #1 also penetrated the DD, EE, and FF sandstones within the lower Miocene interval. The three sandstones were water wet based on the resistivity log, thus the direct pore pressures record the aquifer water phase pressure in the Mad Dog field (**Fig. 2.6**). The water phase gradient in the DD sandstone is 0.442 psi/ft (10.004 MPa/km) or 1.020 g/cc and in the EE and FF sandstones 0.441 psi/ft (9.996 MPa/km) or 1.016 g/cc. The DD sandstone is not in pressure communication with the EE and FF sandstones because the water phase pressures lie on separate gradients.

Using the other well penetrations in the lower Miocene interval the fluid densities were obtained from the direct pore pressure measurements within the three sandstone units (**Table 2.1**). The oil density within the DD sandstone is approximately 0.880 g/cc and the water density is approximately 1.020 g/cc. The oil density within the EE and FF

is approximately 0.876 g/c and the water density is 1.017 g/cc. These respective densities are in the range of the expected oil and water densities. Overall, the water and oil densities between the sandstones are similar but between the DD and the EE/FF sandstones the pressures do not fall on the same gradients within wells. This suggests that the DD and EE/FF sandstones are not in pressure communication.

2.4.2 Integrating pressure and log data for hydrocarbon distribution

Using the fluid gradients and fluid contacts across the Mad Dog field can provide insight into how the lower Miocene interval pressure is connected across the field. The DD sandstone from the pressure data reveals that the sandstone is isolated from the EE and FF sandstones. Knowing this the DD sandstone fluid connectivity will be looked at separately from the EE and FF sandstones. Pore pressure data also reveals that the EE and FF sandstones are in pressure communication. In order to understand how the reservoir sandstones are connected the direct pore pressure measurements and known fluid contacts are plotted on a depth versus excess pressure plot (**Fig. 2.7 and Fig. 2.9**). Excess pressure (u^*) is defined as:

$$u^* = u - \rho_w g z \quad (\text{Eq. 2.1})$$

where u is pore pressure, ρ_w is formation water density, assumed to be 1.075 g/cc (0.47 psi/ft) at Mad Dog, g is the acceleration of gravity, and z is True Vertical Depth Subsea (TVDSS). Normal pressure is calculated by assuming a seawater density of 1.023 g/cc (0.44 psi/ft) from sea-level to seafloor, and formation water density in the sediment column. Within an aquifer, excess pressure is constant, while overpressure depends on water depth. Consequently, excess pressure is the preferred parameter for analyzing reservoir continuity, especially in a field such as Mad Dog, where water depths can vary

by 2000' or more (**Fig. 2.1**). I use a constant water density (ρ_w) of 1.023 g/cc (0.44 psi/ft) from the sea-level to total depth to calculate excess pressures across the field

DD Sandstone

In the DD sandstone, the water phase pressure was measured in well 783 #1 in the northeast fault block where the water gradient is 0.442 psi/ft (10.004 MPa/km). The water phase pressure is extrapolated along its static gradient with depth (**Fig. 2.7**). Wells 782 #1 and 826 #1, in the east fault block measured the oil phase pressure. These measurements line up on a single oil gradient of 0.343 psi/ft (7.751 MPa/km). The oil gradient between the two wells is in agreement with the oil gradients observed within the wells. In the east fault block the OWC is not penetrated, therefore the OWC is projected. The lowest known oil (LKO) in the east fault block was penetrated at 20,425 feet (6,226 meters) in well 826 #3. Assuming that the east and northeast aquifer pressures are in communication, the OWC is projected from the intersection of the water phase pressures and the oil phase pressures. The projected OWC is at 20,503 feet (6,249 meters) in the east fault block.

Plotting the oil phase pore pressures from the south, southwest ridge, and west fault blocks (wells 826 #5, 825 #1-ST1, 825 #4-ST3, and 782 #11-ST1) shows that the oil phase pressures line up on a single gradient of 0.366 psi/ft (8.270 MPa/km). This suggests that the oil column in the south, southwest ridge, and west fault blocks share an OWC and are in pressure communication across the field. In the DD sandstone the OWC was not penetrated in any of the three fault blocks, therefore the OWC is projected. The LKO oil within the three fault blocks is at 22,000 feet (6,706 meters). Assuming that the aquifer pressures in the northeast fault block are in pressure communication with the three fault blocks the OWC can be projected from the water phase pressures and the oil

phase pressures. The projected OWC for the south, southwest ridge, and the west fault block is at 24,062 feet (7,334 meters).

Based on the pore pressure and projected OWC's the oil phase in the east fault block in the DD sandstone is not in pressure communication with the DD sandstone in the south, southwest ridge, and west fault blocks at Mad Dog (**Fig. 2.8**). The oil phase pressures are extrapolated down to the aquifer pressures measured in the northeast fault block, which suggest that the aquifer around the Mad Dog field is in pressure communication in the DD sandstone.

EE/FF Sandstone

In the EE/FF sandstone, the water phase pressure was measured in well 783 #1 in the northeast fault block where the water gradient is 0.441 psi/ft (9.996 MPa/km). The water phase pressure is extrapolated along its static gradient with depth (**Fig. 2.9**). Wells 782 #1 and 826 #1, in the east fault block measured the oil phase pressure. These measurements line up on a single oil gradient of 0.345 psi/ft (7.797 MPa/km). The oil gradient between the two wells is in agreement with the oil gradients observed within the wells. In the east fault block the OWC was penetrated in well 826 #3 at 20,640 feet (6,291 meters). Extrapolating the oil phase pressures down to the penetrated OWC yields a pressure of 12,335 psi (85.05 MPa), which is in agreement with the water phase pressure from the northeast fault block at 12,339 psi (85.07 MPa). This suggests that aquifer between the northeast and east fault block are in pressure communication.

Plotting the oil phase pore pressure from the south, southwest ridge, and west fault blocks (wells 826 #5, 825 #4-ST3, and 782 #11-ST1) shows that the oil phase pressures line up on a single gradient of 0.370 psi/ft (8.363 MPa/km). This suggests that the oil column between the south, southwest ridge, and west fault blocks are in pressure communication across the field. The OWC was penetrated in the west fault block at

23,330 feet (7,111 meters) in well 781 #11. The LKO in the southwest ridge fault block was 22,000 feet (6706 meters) and the LKO in the south fault block was at 23,464 feet (7,152 meters) (**Fig. 2.10**). Based on the OWC in the west block and the LKO in the south block suggest that there are multiple OWC's that exists between the west and south fault blocks. From the OWC in the west fault block at 23,330 feet (7,111 meters) a second aquifer pressure is extrapolated with depth and the inferred aquifer pressure is 62 psi (0.43 MPa) higher with depth than the aquifer pressure measured in the northeast fault block.

Assuming that the aquifer pressure between the northeast and south fault blocks are in pressure communication, the OWC can be projected from the water and oil phase gradients. This yields a projected OWC of 24,204 feet (7,377 meters) in the south fault block. If the aquifer between the northeast and south fault blocks are not in pressure communication an inferred aquifer gradient can be assumed from an OWC, where the OWC would have to be at least below the LKO at 23,464 feet (7,152 meters).

The LKO (22,000 feet, 6,706 meters) in the southwest ridge fault block is above the penetrated OWC (23,330 feet, 7,111 meters) in the west fault block and above the LKO (23,464 feet, 7,152 meters) in the south fault block. From these observations there are several possible scenarios that could exists for how the southwest ridge fault block is in pressure communication between the west and south fault blocks. First, assuming that the southwest ridge fault block has the same OWC as the west fault block, the aquifer pressure between southwest ridge and west fault blocks would be in pressure communication and not in pressure communication with the south fault block. Second, the southwest ridge and south fault blocks could have the same OWC, thus having the same aquifer pressure between the two fault blocks. The aquifer pressure in the west fault block would not be in pressure communication in the southwest ridge and south fault

blocks if the OWC was the same. Lastly, the southwest ridge fault block could have an OWC different than the south and west fault blocks. This would suggest that there would be three separate aquifer pressures that would not be in pressure communication between the south, southwest ridge, and west fault blocks.

2.5 DISCUSSION

Based on the pressure distribution, fluid contacts, and reservoir structure the fluid distribution can be estimated in the various sandstones within the lower Miocene interval. The DD sandstone is not in pressure communication with EE/FF sandstone due to the presence of a thick mudstone (~75 feet, 23 meters) separating the DD and EE sandstones. In the DD sandstone there were no fluid contacts penetrated, therefore the OWCs were projected from the oil and water phase pressures. Based on these projections the oil phase pressure within south, southwest ridge, and west fault blocks are in pressure communication and the east fault block is not in pressure communication with these fault blocks. The aquifer pressure measured in the northeast fault block was used as a reference aquifer pressure throughout the field. In order to prove this assumption, an OWC would need to be penetrated or direct pore pressure measurements in the water phase would need to be made either in the south, southwest ridge, or west fault block.

The EE/FF sandstone provides a more accurate prediction of hydrocarbon distribution since multiple OWCs were penetrated. The pore pressure measurements in the EE/FF sandstone show that the oil phase pressures within the south, southwest ridge, and west fault blocks are in pressure communication and are separated from the east fault block. The aquifer pressure between the northeast and east fault blocks are in pressure communication. The aquifer pressure within the west, southwest ridge, and west fault blocks is unknown, but projected aquifer pressures were determined from oil phase

pressures and OWCs. Since the west penetrated an OWC (23,330 feet, 7,111 meters) above the LKO (23,464 feet, 7,152 meters) in the south, there are multiple OWC's that exist between the south and west fault blocks. This infers that the aquifer pressure between the west and south fault blocks are not in pressure communication and Fault 1 or Fault 2 at southwest ridge separate the aquifer into different compartments. In order to determine which fault is causing different aquifer pressures in the south and west fault block, an OWC or water phase pressures would need to be determined in the southwest ridge fault block.

The EE/FF sandstone has multiple aquifer phase pressures that exist throughout the field and there are several possible explanations for this occurrence. A previous study before the south fault block was drilled inferred a tilted OWC at Mad Dog due to regional hydrodynamic aquifer caused by mechanical compaction and dewatering of large column of sediments (Dias et al., 2009). This is plausible, but in order to accurately test this hypothesis more penetrations of the OWC around the field would need to be known. There are only 2 OWC's penetrated in the EE/FF sandstone. If 2 more OWCs were penetrated in the EE/FF sandstone this could prove or disprove the presence of a tilted OWC across the field. Another explanation is that the normal faults segment the aquifer and that within the oil phase the sandstones are leaking, which is causing the south, southwest ridge, and west fault blocks within the oil column to be in pressure communication. In order to prove whether the reservoir within the oil column is leaking across the faults is to use production data and determine whether pressures equilibrate across the faults. If the pressures within the south, southwest ridge, and west fault blocks do not equilibrate with increasing production, then the faults either are not leaking or on production timescales the reservoir cannot equilibrate.

2.6 CONCLUSION

In order to define the static reservoir compartments, the fluid contacts and pressure measurements within the reservoir structure are analyzed. This is critical for delineating hydrocarbon distribution and connectivity. The pressure data shows that the DD and EE/FF sandstones within the lower Miocene interval are not in pressure communication across the field due to the presence of thick mudstone between the DD and EE sandstones. By combining the reservoir structure, pressure data, and fluid contacts at Mad Dog, there are two aquifer phase pressure in the EE/FF sandstones and two oil phase pressures that exist both in the DD and EE/FF sandstones across the field. These multiple aquifer and oil phase pressures are attributed to the normal faults around the field that compartmentalize the lower Miocene reservoir in the Mad Dog field.

2.7 FIGURES

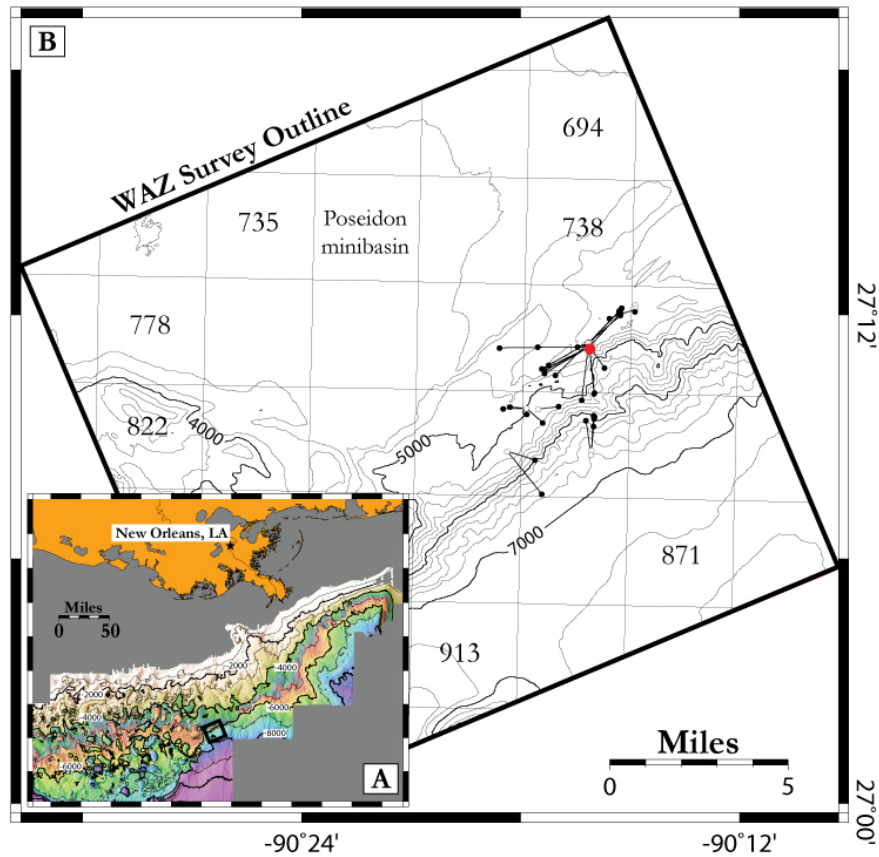


Figure 2.1: Location and base map of the Mad Dog field, Gulf of Mexico

(A) The Mad Dog field is located approximately 190 miles (306 kilometers) southwest of New Orleans. The seafloor topography illustrated with 200 feet contours from NOAA bathymetry data. (B) The black outline represents the 3D wide azimuth seismic survey (WAZ). The seafloor topography illustrated with 100 feet contours from the WAZ survey. The open white circles represent the surface well locations and the black dots represent the bottom hole locations. The appraisal well 782 #1 is shown with the red dot.

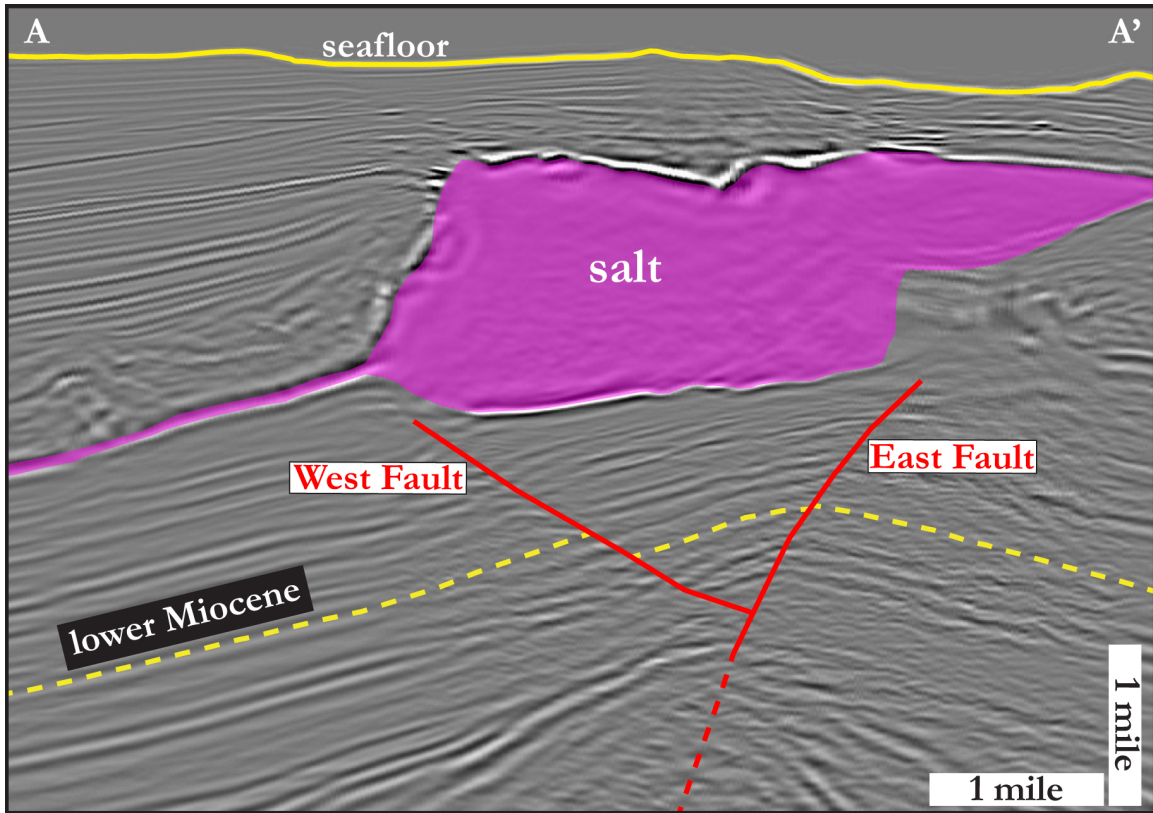


Figure 2.2: Regional seismic line across the Mad Dog structure

A seismic cross section across the central region of the Mad Dog field showing the regional anticline structure of the subsalt sediments. The lower Miocene reservoir horizon was mapped on a zero phase reflector and is shown with the dashed yellow line. The two main east and west normal faults are shown in red. Cross section A-A' location is shown in Figure 2.3. Seismic data courtesy of BP, BHP Billiton, and Chevron.

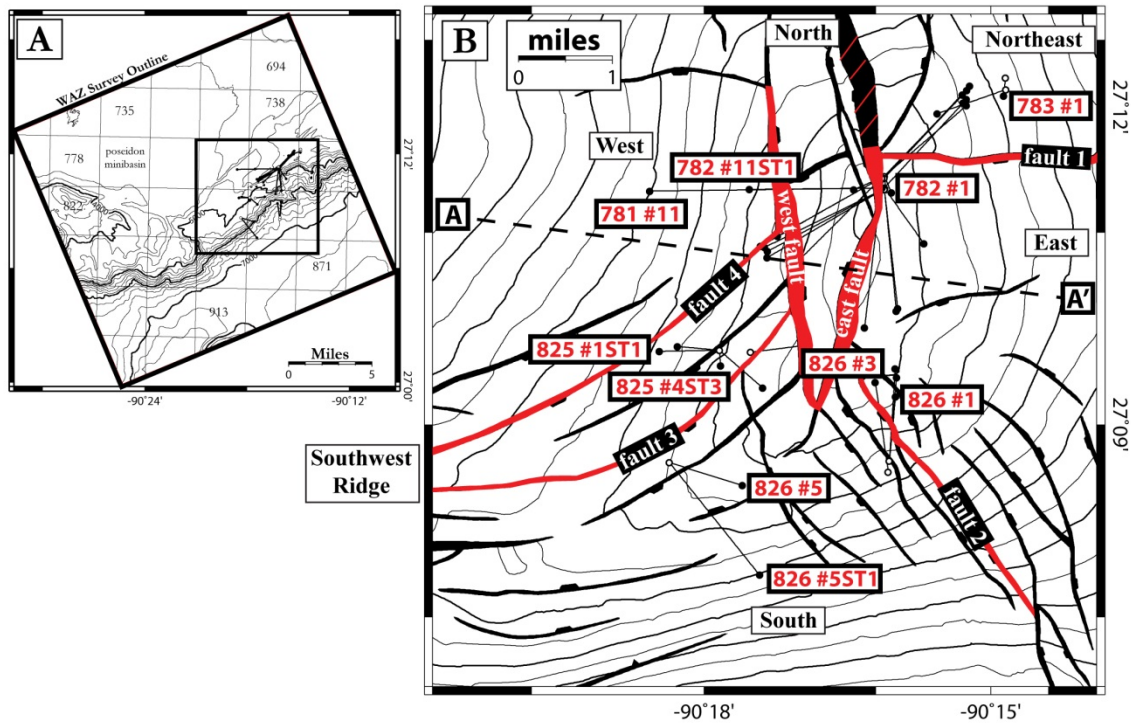


Figure 2.3: Structure map of the lower Miocene sandstone

(A) The black outline represents the 3D wide azimuth seismic survey (WAZ). The seafloor topography illustrated with 100 feet contours from the WAZ survey. The inner black outline represents the area of the lower Miocene structure map to the right. (B) Structure map of the lower Miocene sandstone across the Mad Dog field from the WAZ survey illustrated with 500 feet contours. The surface location locations are shown with small white circle and bottom hole locations are noted by the larger black circles. The black polygons are vertical projections of the fault plane onto the lower Miocene Top horizon: the downthrown side of the fault is marked with black bars. The faults shown in red outline the fault block boundaries where the fault blocks are termed the northeast, east, south, southwest ridge, and west fault blocks. The location of the cross section shown in Figure 2.2 is annotated A-A'. Fault polygons provided by BP.

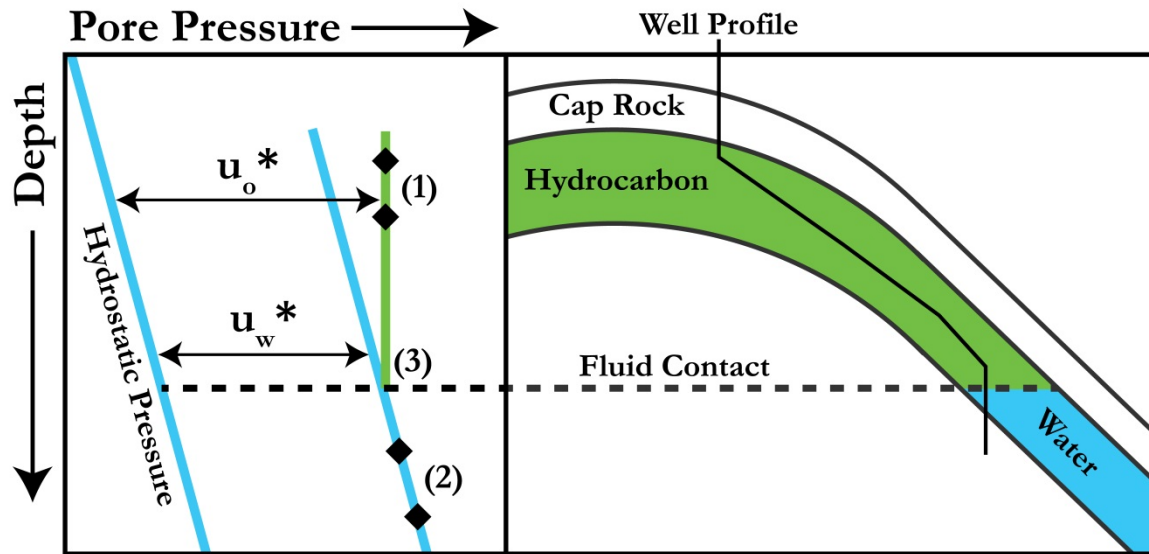


Figure 2.4: Schematic diagram showing the technique to characterize reservoir connectivity throughout the field

The diagram shows an example of how a structure with multiple fluids is in pressure communication. (1) In-situ pore pressure (black diamonds) within the hydrocarbon phase. A static hydrocarbon gradient can be extrapolated vertically from the pore pressure measurements. (2) In-situ pore pressure (black diamonds) within the water phase. A static water gradient can be extrapolated vertically from the pore pressure measurements. (3) At the fluid contact the water and hydrocarbon phase pressure are assumed to be equal. Note that if the fluid contact is not penetrated by a wellbore then the fluid contact can be projected from the static gradients in the water and hydrocarbon phases. u_o^* = oil phase overpressure and u_w^* = water phase overpressure.

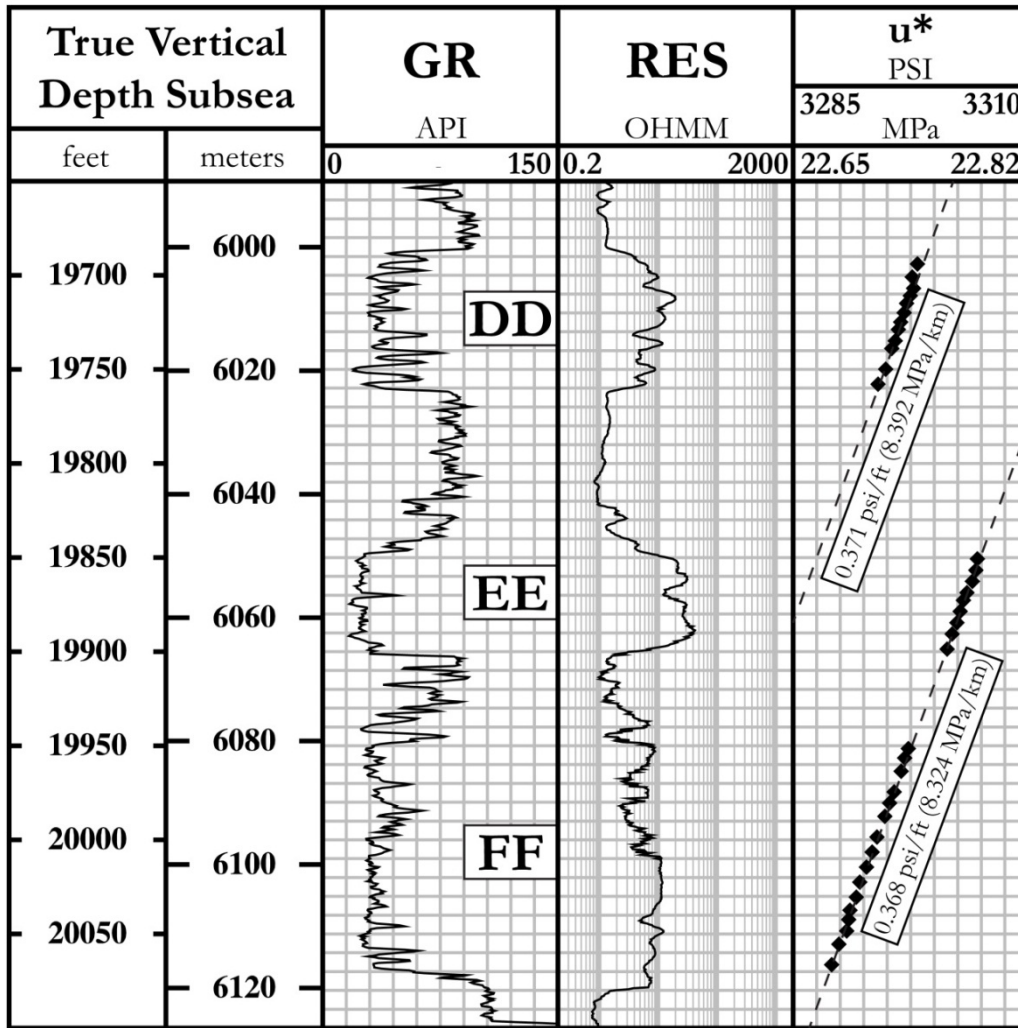


Figure 2.5: Type log of the lower Miocene reservoir sands at Mad Dog field from well 782-1

The direct pore pressure measurements (black diamonds) within DD, EE, and FF sandstones within the lower Miocene reservoir recorded the oil phase pressure based on the high resistivity which indicates oil. The DD sandstone lies on a separate oil gradient than the EE and FF sandstones suggesting the sandstones are not in pressure communication. The DD sandstone has an oil gradient of 0.371 psi/ft (8.392 MPa/km) and the EE/FF sandstones have an oil gradient of 0.368 psi/ft (8.324 MPa/km). The excess pressure (u^*) was calculated by subtracting the absolute pressures/stresses from the integration of a constant water density of 1.023 g/cc (0.44 psi/ft) from the seafloor to the total depth.

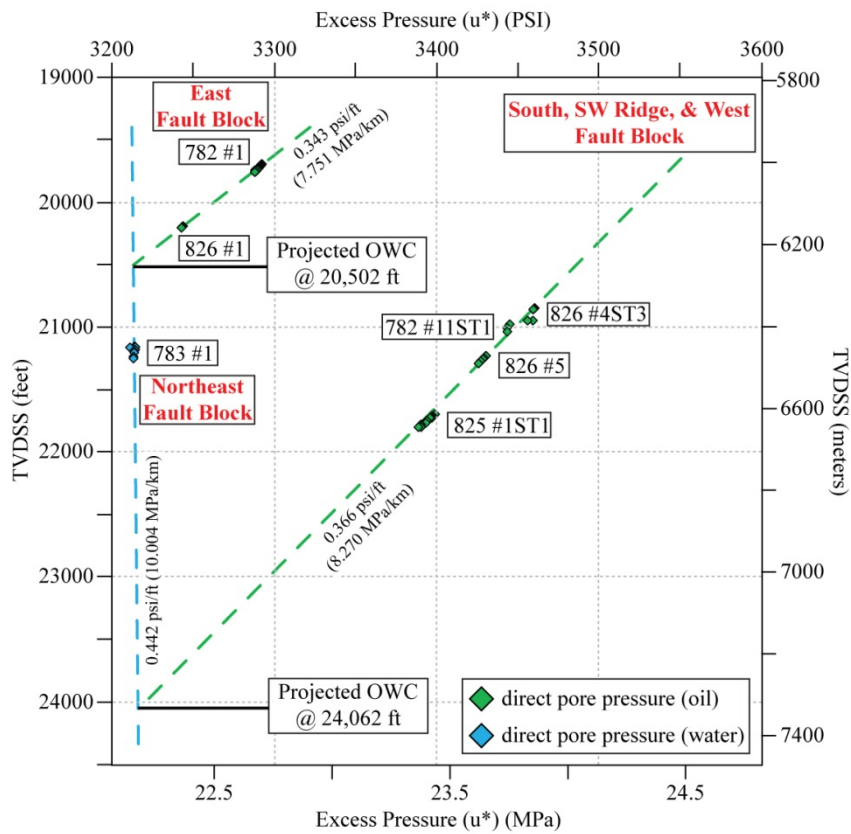


Figure 2.7: Pore pressure versus depth plot for the DD sandstone

The water phase pressure was measured in well 783 #1 in the northeast fault block with a gradient of 0.442 psi/ft (10.004 MPa/km). Wells 782 #1 and 826 #1 line up on a single oil gradient of 0.343 psi/ft (7.751 MPa/km) in the east fault block. The projected OWC in the east fault block yields 20,502 feet (6,249 meters). Wells 826 #5, 826 #4ST3, 825 #1ST1, and 782 #11ST1 line up on a single oil gradient of 0.366 psi/ft (8.27 MPa/km). The projected OWC within the south, southwest ridge, and west fault blocks yields 24,062 feet (7,334 meters). The excess pressure (u^*) was calculated by subtracting the absolute pressures/stresses from the integration of a constant water density of 1.023 g/cc (0.44 psi/ft) from the seafloor to the total depth.

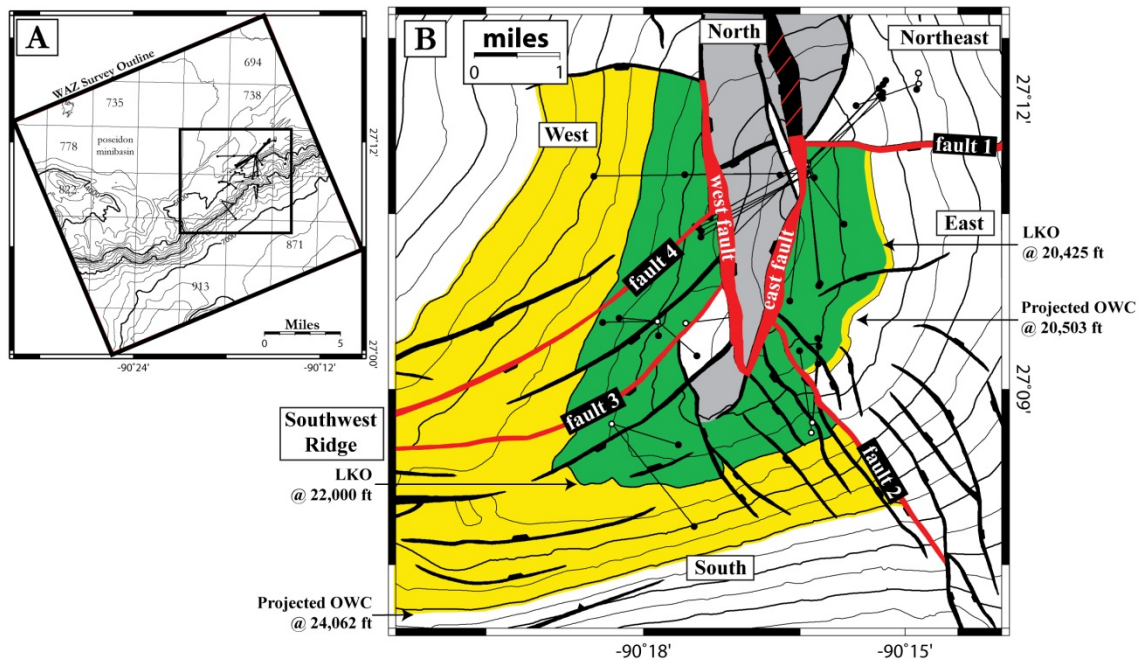


Figure 2.8: Structure map of the DD sandstone and the fluid distribution at Mad Dog

(A) The black outline represents the 3D wide azimuth seismic survey (WAZ). The seafloor topography illustrated with 100 feet contours from the WAZ survey. The inner black outline represents the area of the lower Miocene structure map to the right. (B) Structure map of the lower Miocene sandstone across the Mad Dog field from the WAZ survey illustrated with 500 feet contours. The surface location locations are shown with small white circle and bottom hole locations are noted by the larger black circles. The red normal faults interpreted as pressure barriers and hashed red normal faults are possible pressure barriers. These normal faults define the various regions around the Mad Dog field that divide the reservoir into separate compartments. The various fluids within the DD sandstone is shown with green representing oil, yellow representing inferred oil, gray is unknown fluid, and white is water. OWC = oil water contact and LKO = lowest known oil. Fault polygons provided by BP.

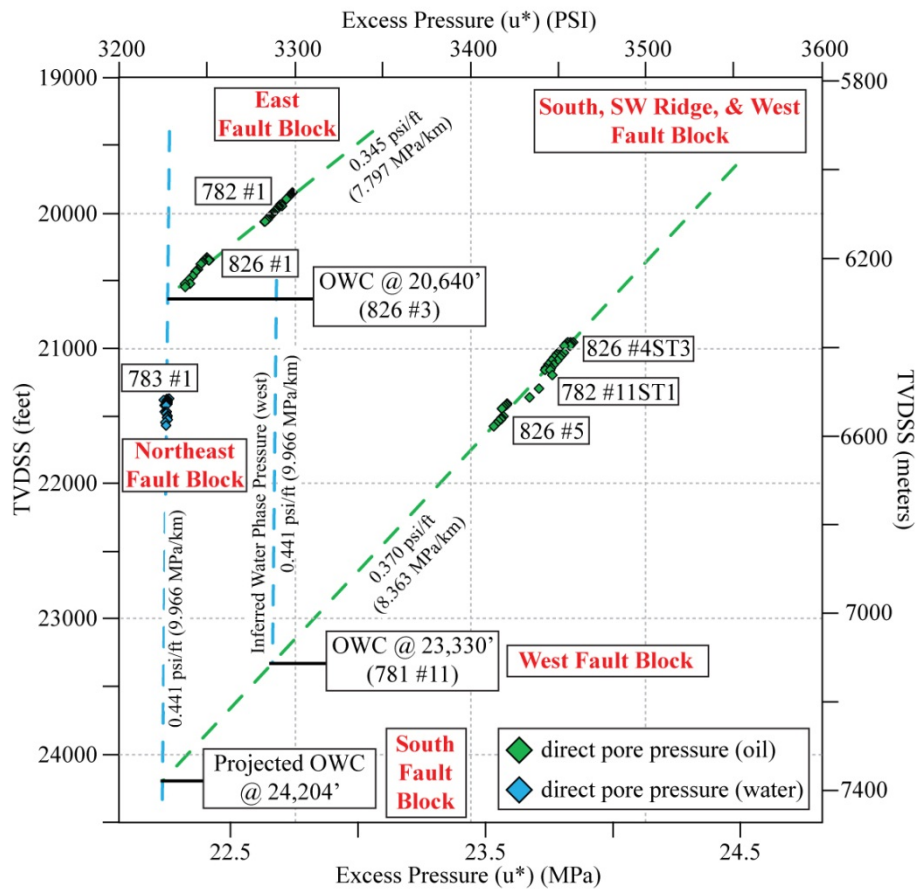


Figure 2.9: Pore pressure versus depth plot for the EE/FF sandstone

The water phase pressure was measured in well 783 #1 in the northeast fault block with a gradient of 0.441 psi/ft (9.966 MPa/km). Wells 782 #1 and 826 #1 line up on a single oil gradient of 0.345 psi/ft (7.797 MPa/km). The oil water contact (OWC) was penetrated in well 826 #3 and projecting the water phase and oil phase pressures to the OWC suggests that wells 783 #1, 782 #1, 826 #1, and 826 #3 in pressure communication. Wells 826 #5, 826 #4ST3 and 782 #11ST1 line up on a single oil gradient of 0.370 psi/ft (8.363 MPa/km). Multiple water phase pressures exists because projecting the water phase pressure from wells 783 #1 and the oil phase pressure down with depth suggests a projected OWC of 24,204 feet (7,378 meters) and the penetrated OWC was at 23,330 feet (7,102 meters) in the west fault block.

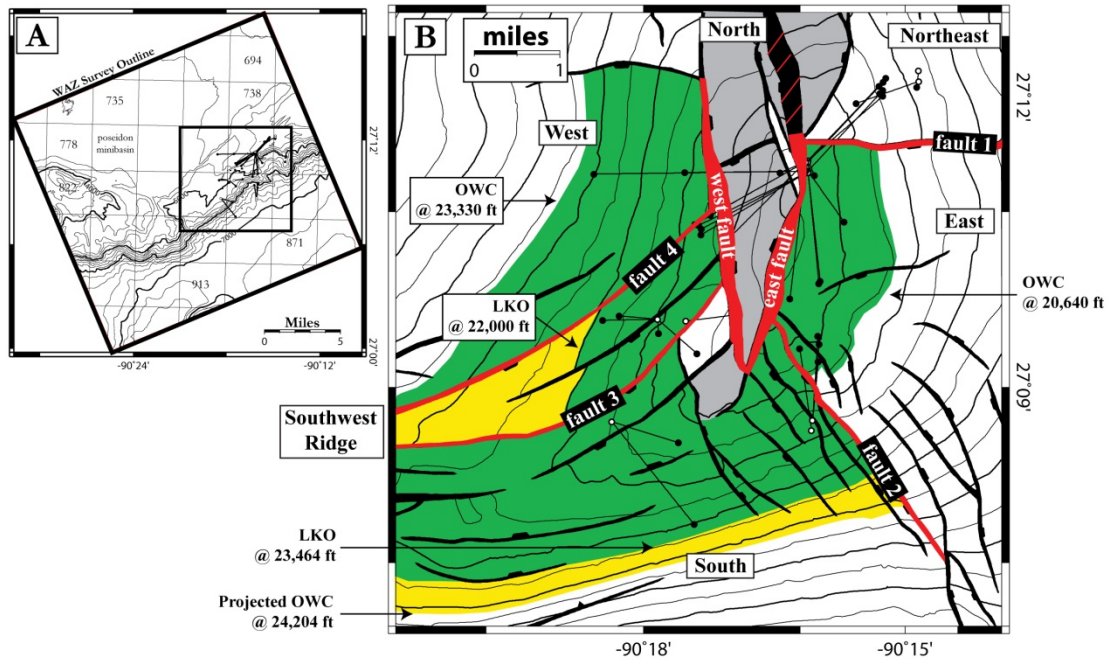


Figure 2.10: Structure map of the EE/FF sandstone and the fluid distribution at Mad Dog

(A) The black outline represents the 3D wide azimuth seismic survey (WAZ). The seafloor topography illustrated with 100 feet contours from the WAZ survey. The inner black outline represents the area of the lower Miocene structure map to the right. (B) Structure map of the lower Miocene sandstone across the Mad Dog field from the WAZ survey illustrated with 500 feet contours. The surface location locations are shown with small white circle and bottom hole locations are noted by the larger black circles. The red normal faults interpreted as faults that act as pressure barriers and dashed red normal faults are possible pressure barriers. These normal faults define the various regions around the Mad Dog field that divide the reservoir into separate compartments. The various fluids within the EE/FF sandstone is shown with green representing oil, yellow representing inferred oil, gray is unknown fluid, and white is water. Fault polygons provided by BP.

2.8 TABLES

Well Name	Fault Block	Sandstone	TVDSS Top	TVDSS Bottom	Gradients		Density	Fluid Type
			<i>feet</i>	<i>meters</i>	<i>PSI/ft</i>	<i>MPa/km</i>	<i>g/cc</i>	
783 #1	Northeast	DD	21,147	21,529	0.442	10.004	1.020	Water
		EE	21,363	21,427	0.441	9.966	1.016	Water
		FF	21,442	21,606	0.441	9.966	1.016	Water
782 #1	East	DD	19,685	19,764	0.371	8.392	0.856	Oil
		EE	19,838	19,903	0.368	8.324	0.849	Oil
		FF	19,928	20,081	0.368	8.324	0.849	Oil
826 #1	East	DD	20,173	20,220	0.368	8.324	0.849	Oil
		EE	20,325	20,386	0.382	8.641	0.881	Oil
		FF	20,405	20,549	0.382	8.641	0.881	Oil
826 #5	South	DD	21,207	21,296	0.366	8.279	0.844	Oil
		EE	21,396	21,446	0.406	9.184	0.937	Oil
		FF	21,509	21,655	0.406	9.184	0.937	Oil
825 #1ST1	Southwest Ridge	DD	21,800	21,890	0.350	7.917	0.807	Oil
		EE	Faulted Out					
		FF	Faulted Out					
826 #4 ST3	Southwest Ridge	DD	20,910	20,960	0.417	9.433	0.962	Oil
		EE	21,040	21,080	0.378	8.551	0.872	Oil
		FF	21,130	21,270	0.378	8.551	0.872	Oil
782 #11 ST1	West	DD	20,968	21,053	0.418	9.455	0.964	Oil
		EE	21,168	21,233	0.364	8.234	0.840	Oil
		FF	21,296	21,457	0.364	8.234	0.840	Oil

Table 2.1: Summary table of the pore pressure gradients and densities in the lower Miocene sandstone across the field

Fault Blocks	Gradients		Density	Fluid Type	Depth @ OWC		Pressure @ OWC	
	PSI/ft	MPa/km	g/cc		feet	meters	PSI	MPa
Northeast	0.442	10.004	1.020	Water	N/A		N/A	
East	0.343	7.751	0.790	Oil	20503*	6249	12263	84.6
South, SW Ridge and West	0.366	8.270	0.843	Oil	24062*	7334	13837	95.4

*Projected OWC from Pressures

Table 2.2: Summary table of the pore pressure gradients, fluid contacts, and pressures at the fluid contacts between the fault blocks in the DD sandstone

Fault Blocks	Gradients		Density	Fluid Type	Depth @ OWC		Pressure @ OWC	
	PSI/ft	MPa/km	g/cc		feet	meters	PSI	MPa
Northeast	0.441	9.966	1.016	Water	N/A		N/A	
East	0.345	7.797	0.795	Oil	12335	3760	12335	85.0
West	0.441	9.966	1.016	Inferred Water	23330	7111	13586	93.7
South, SW Ridge and West	0.370	8.363	0.853	Oil	24204*	7377	13909	95.9

*Projected OWC from Pressures

Table 2.3: Summary table of the pore pressure gradients, fluid contacts, and pressures at the fluid contacts between the fault blocks in the EE/FF sandstone

Chapter 3: Subsalt Pressure Prediction in the Miocene Mad Dog Field, Gulf of Mexico

ABSTRACT

Sandstone pressures follow the hydrostatic gradient in Miocene strata of the Mad Dog field, deepwater Gulf of Mexico, while pore pressures in the adjacent mudstones track a trend from well-to-well that can be approximated by the total vertical stress gradient. The sandstone pressures within these strata are everywhere less than the bounding mudstone pore pressures and the difference between them is proportional to the total vertical stress. The mudstone pressure is predicted from its porosity with an exponential porosity vs. vertical effective stress relationship where porosity is interpreted from wireline velocity. Sonic velocities in mudstones bounding the regional sandstones fall within a narrow range throughout the field from which we interpret their vertical effective stresses can be approximated as constant. We show how to predict sandstone and mudstone pore pressure in any offset well at Mad Dog given knowledge of the local total vertical stress. At Mad Dog, the approach is complicated by the extraordinary lateral changes in total vertical stress that are caused by changing bathymetry and the presence/absence of salt. A similar approach can be used in other sub-salt fields. We suggest that pore pressures within mudstones can be systematically different from that of the nearby sandstones and that this difference can be predicted. Well programs must ensure that the borehole pressure is not too low, which results in borehole closure in the mudstone intervals, and not too high, which can result in lost circulation to the reservoir horizons.

3.1 INTRODUCTION

Fluid overpressure is pressure that is greater than the hydrostatic pressure for pore water in hydraulic communication with the surface, termed “normal pressure”. Overpressures are present in sedimentary basins around the world. They are of importance to the petroleum industry for exploration, development, production, and drilling and well completions (Fertl et al., 1994). Understanding of the overpressure behavior with depth is of importance for economic and safety reasons.

Overpressure development in deep-water Gulf of Mexico basins is driven primarily by compaction disequilibrium (Bredehoeft and Hanshaw, 1968; Harrison and Summa, 1991; Hart et al., 1995; Sharp and Domenico, 1976). Overpressure develops if the sediment’s pore fluid cannot expel freely because the permeability is too low. If the pore fluid is able to drain water freely, the fluid pressure is at normal pressure.

Predicting accurate pore pressures can greatly enhance the design of casing programs and mud weight requirements for new wells. If pore pressure is not accurately predicted it can lead to drilling hazards such as blowouts, loss of circulation, kicks, and hole instability (Sweatman et al., 1999). Salt systems add geologic and geophysical complexity that can make pore pressure prediction difficult, and subsalt drilling expensive and challenging (Rohleder et al., 2003; Sweatman et al., 1999; Whitson and McFadyen, 2001; Willson and Fredrich, 2005).

Pore pressure is commonly predicted using interval velocities derived from seismic data, but extracting accurate subsalt velocities can be difficult due to the high velocity contrasts between salt and the surrounding sediment. This causes the velocities from the seismic data to be obscured; therefore pore pressure prediction is less accurate because the velocities are not reliable. Potential sources of velocity errors below salt include poor seismic data quality, processing, anisotropy, and low resolution (Viceer et

al., 2006). Drilling through the base of salt can be further complicated by uncertainties in how fluid pressures, sediment stresses, and the salt are interacting. Nearly 50% of the wells in the Gulf of Mexico have encountered problems exiting the base of salt (Viceer et al., 2006). In addition to kicks and drilling fluid losses, wellbore instability due to high shear stress may also be encountered (Sweatman et al., 1999). There have been geomechanical models describing pore pressure and stress variations that maybe present near salt bodies (Luo et al., 2012a; Nikolinakou et al., 2011; Nikolinakou et al., 2012).

We study the subsalt Mad Dog field in the deep-water Gulf of Mexico (**Fig. 3.1**). We first characterize the in-situ pore pressure signature across the field. A porosity-vertical effective stress relationship is developed from shallow Pleistocene strata to predict the pore pressure across the field. We interpret that sandstone and adjacent mudstone pressures are not in pressure equilibrium within the Miocene strata. The sonic velocities of mudstones bounding the regional sandstones fall within a narrow range, from which we conclude the vertical effective stress can be approximated as constant. We show that the mudstone pressures increase with increasing total vertical stress. This implies that given knowledge of the vertical effective stress from an offset well and total vertical stress in a new well location, the mudstone pressure in the new well location can be determined.

3.2 OVERVIEW OF THE MAD DOG FIELD

The Mad Dog field lies below an allochthonous salt sheet beneath the Sigsbee Escarpment in deep-water Gulf of Mexico. It is located in Green Canyon (GC) blocks 781, 782, 825, and 826, 190 miles (306 kilometers) southwest of New Orleans in 4,000 feet (1,219 meters) to 7,000 feet (2,134 meters) of water (**Fig. 3.1**). The field extends across the Sigsbee Escarpment, which represents the surface and seaward-most indicator

of the mobile salt in the northern Gulf of Mexico (Gealy, 1955). The field lies within a north-south trending anticline and is a faulted, four-way closure. Production is largely from lower Miocene turbidite sandstones (**Fig. 3.2**) that are present throughout the Mad Dog field both in subsalt and outboard of salt sections. The estimated gross reserves are up to four billion barrels of oil equivalent (Gismatullin, 2011). Production began in 2005 with production in June 2012 of over 100 million barrels.

3.3 PORE PRESSURES AT MAD DOG

3.3.1 Approach

We characterize pore pressure as pressure, excess pressure, pressure gradient, and equivalent mud weight (**Fig. 3.3**). Excess pressure (u^*) is defined as:

$$u^* = u - \rho_w g z, \quad (\text{Eq. 3.1})$$

where u is pore pressure, ρ_w is formation water density, g is the acceleration of gravity, and z is True Vertical Depth Subsea (TVDSS) (**Fig. 3.3a**). The quantity $\rho_w g z$ will be termed “hydrostatic pressure” (u_h). Normal pressure (u_n) is calculated by assuming a seawater density of 1.023 g/cc (0.44 psi/ft) from sea-level to seafloor, and formation water density in the sediment column. Within an aquifer, excess pressure ($u-u_h$) is constant, while overpressure ($u-u_n$) depends on water depth. Consequently, excess pressure is generally the preferred parameter for analyzing reservoir continuity, especially in fields where water depths vary significantly. However, pressure measurements in the sandstones at Mad Dog indicate the formation water has the same density as seawater. Therefore, a constant formation water density (ρ_w) of 1.023 g/cc (0.44 psi/ft) was assumed across the field, which, in turn, makes overpressure equal to excess pressure (**Fig. 3.3b**). The total vertical stress (σ_v) is calculated by integrating the wireline bulk density (ρ_{bulk}) log with depth (**Appendix A**).

$$\sigma_v = \int \rho_{bulk} g dz \quad (\text{Eq. 3.2})$$

Pressure gradients can be expressed as either the local slope, du/dz , or average slope, u/z' , where z' is true vertical depth below a given datum. The first is used to determine pore fluid densities from reservoir pressure measurements. The second is another way of characterizing pore pressure magnitudes. As used in this paper, the term “pressure gradient” implies the average slope. The average slope also defines the density of a uniform column of drilling fluid starting at the datum must have to just balance the pressure, termed the “equivalent mud weight” (EMW): (**Fig. 3.3c**):

$$EMW = \frac{u}{gz} \quad (\text{Eq. 3.3})$$

When we use the term mud weight our datum is from the sea-surface and not the rig floor or the kelly bushing. The most frequently used conversion factors between pressure gradient and EMW are: 0.434 psi/ft = 9.81 MPa/km = 8.34 lbs/gal (ppg) = 1.0 g/cc.

In the permeable sandstone bodies, both water and hydrocarbon pressures are assumed to follow their static pressure gradients, respectively (**Fig. 3.3**). When hydrocarbons are present in the reservoir, the water phase pressures are interpreted by projecting the measured hydrocarbon pressures down to the hydrocarbon-water contact along the static pressure gradient of the hydrocarbon phase (e.g. 0.33 psi/ft for oil).

3.3.2 Mad Dog

The Mad Dog discovery well 826 #1 drilled in 1999 was drilled outboard of the Sigsbee Escarpment where no salt is present (**Fig. 3.4**). The well drilled through Pleistocene aged sediments from the seafloor to 15,500 feet (4,724 meters), ultimately reaching a total depth of 20,500 feet (6,248 meters) in lower Miocene strata. It is the only well for which we have direct pore pressure measurements in the shallower Pleistocene strata as well as in the deeper section.

Pore pressure measurements in Pleistocene strata have a relatively low and nearly constant excess pressure of 900 psi (6.21 MPa) (open circles, **Fig. 3.4e**). The constant excess pressure implies that these sandstones are hydraulically connected. The gamma ray and resistivity logs (**Fig. 3.4a, b**) show that this is a sandstone prone section, which supports the hypothesis that the sandstones are hydraulically interconnected. Furthermore, it is capped by a mudstone that may act to seal in the excess pressure within this section. Between the base of the Pleistocene and the top of the upper Miocene, the excess pressure rises significantly to 2,550 psi (17.58 MPa) (from 9.5 to 11.1 ppg). This increase in excess pressure with depth occurs over an interval where there is less sand interbedded with the mudstone as indicated by the gamma ray log (**Fig. 3.4a**). Excess pressure decreases with depth from the top of the middle Miocene strata to the middle of the middle Miocene strata before it rises again towards the base of the well in the lower Miocene strata (**Fig. 3.4e**). The major reservoir in the lower Miocene strata lies at 20,000 feet (6,100 meters) and is in the location of where the pore pressure starts to rise. This interval is extremely sand-prone.

The 782 #1 well (**Fig. 3.5**) was drilled in 1999 and was the first subsalt well at Mad Dog. It penetrated 5,000 feet (1,524 meters) of salt. At the base of salt at 15,300 feet (4,663 meters), there was a pore pressure kick that necessitated setting a casing string and increasing the mud weight from 12.9 to 13.9 ppg. In this well, direct pressure measurements were only made in the Miocene strata. As in the 826 #1 well (**Fig. 3.4**), the pore pressure drops from the upper to middle Miocene strata before reaching a minimum in the base of the middle Miocene strata and then rising in the sand-prone lower Miocene strata.

In the Mad Dog region, we were able to map 4 sandstone horizons that also had direct pressure measurements made within them to characterize the pressures. The 4

sandstone horizons are termed the N, PQRS, V, and the DD, EE, and FF sandstones (Walker et al., 2012). Within those four horizons, we found that the water phase excess pressure were approximately constant (i.e. pressures within each horizon fall along a static pressure gradient), which indicates that these sandstone bodies are permeable and well-connected aquifers. Appendix D presents the details of this analysis. The pressure results for each horizon are presented in Table 3.2 and they are presented on each pressure depth plot (e.g. Fig. 3.4e, 3.5e, 3.9e, and 3.10e).

In summary, there is a characteristic pressure signature at Mad Dog. Pore pressure rises from the Pleistocene to the upper Miocene strata and then decreases between the upper and middle Miocene strata before reaching a minimum in the middle/base of the middle Miocene strata (**Figs. 3.4, 3.5**). Pore pressure then rises in the lower Miocene strata. Individual sandstones within these strata are hydraulically connected and their constant excess pressure can be mapped across the field. This pore pressure signature is broadly repeated in a range of fields in the Green Canyon region including Pony (GC 468), K2 (GC 562), Knotty Head (GC 512), Spa Prospect (Walker Ridge 285), and Shenzi (GC 609). (Fredrich et al., 2007; Rohleder et al., 2003; Sanford et al., 2006; Weatherl, 2010; Williams et al., 2008). One explanation for the low excess pressure observed in the middle Miocene strata is that these sandstones could be bled-off at a shallower depth in the southern Green Canyon region. The most likely source of where the sandstone are being bled-off is at Green Knoll, which represents an isolated salt diapir rising seaward of the Sigsbee Escarpment where brine vents have been documented (Aharon et al., 1992).

3.4 RELATIONSHIP BETWEEN MUDSTONE POROSITY AND VERTICAL EFFECTIVE STRESS AT MAD DOG

We next study the relationship between mudstone porosity and effective stress to estimate the in-situ pressures within the mudstones at Mad Dog.

3.4.1 Development of a predictive relationship

To predict pore pressure, we develop a relationship between the mudstone porosity and the vertical effective stress. We assume that porosity (n) is proportional to vertical effective stress (σ'_v):

$$n = n_0 e^{-\beta \sigma'_v}, \quad (\text{Eq. 3.4})$$

where n_0 is a reference porosity and β is the compression coefficient. Equation 4 is a common expression used to describe the compression of mudstones (Athy, 1930; Hart et al., 1995; Rubey and Hubbert, 1959). The vertical effective stress (σ'_v) is the total vertical stress (σ_v) less the pore pressure (u):

$$\sigma'_v = \sigma_v - u. \quad (\text{Eq. 3.5})$$

To constrain pore pressure (u) we need to determine vertical effective stress through equation 3.4 and total vertical stress (σ_v). To constrain σ_v , we integrated the total vertical stress as measured by the density log (**Appendix A**). Three factors control total vertical stress at Mad Dog: 1) the water depth (**Fig. 3.1**), 2) the thickness of salt penetrated, and 3) the depth of any individual horizon below the sea floor. Water depth or bathymetry varies greatly at Mad Dog because the field lies beneath the Sigsbee Escarpment and wells have been drilled both in front of and on top of the escarpment (**Fig. 3.6a, b**). For example well 826 #1 is at a water depth of 6,560 feet (2,000 meters), yet well 782 #1 is at 4,423 feet (1,348 meters). Wells that penetrate inboard of the Sigsbee Escarpment (e.g. 783 #1 and 782 #1) have much lower water depth and a thicker sediment column. This results in a higher stress at a given depth below sea-level for these

wells relative to those wells outboard of the Sigsbee escarpment (e.g. the 826 #1). The effect of salt thickness is shown most clearly when total vertical stress is calculated from the seafloor (**Fig. 3.6c, d**). The 783 #1 penetrated the thickest section of salt and thus its total vertical stress calculated from seafloor is less than the wells that penetrated no salt (e.g. the 826 #1). Not surprisingly, where salt is present, the water depth is shallower (**Fig. 3.6a, b**). Ultimately, because water depths at Mad Dog span such a wide range, the overriding control on the total vertical stress at a given depth below sea-level (**Fig. 3.6a, b**) is the water depth: those wells with less water depth have a higher stress.

Once total vertical stress is known, pore pressure can be predicted if the mudstone porosity is known (Eq. 3.4). Mudstone porosities are calculated from the sonic log in the following manner. First, mudstone values were manually picked approximately every 30 feet (9 meters) to 40 feet (12 meters) based on the gamma ray log. A particular sonic velocity was chosen only if the gamma ray and resistivity log together indicated a mudstone interval. This removes the effect of high radioactive zones that are not characteristic mudstones. Where the mudstones were picked, a moving average of 11 samples was taken on the sonic log in order to smooth out the data to eliminate noise from borehole effects or small lithology changes. In other words, for each mudstone that was picked, 5 sonic log values from the picked mudstones above and below are averaged. The typical thickness of the averaging window is 400 feet (122 meters) on given mudstone pick.

These sonic log values were used to calculate the mudstone porosity (n) through an empirical relationship from Issler (1992):

$$n = 1 - \left(\frac{\Delta t_{ma}}{\Delta t} \right)^{1/x}, \quad (\text{Eq. 3.6})$$

where Δt_{ma} is the matrix travel time, Δt is the log-derived travel time, and x is an acoustic formation factor. Issler (1992) determined that $\Delta t_{ma} = 67 \mu\text{s}/\text{ft}$ and $x = 2.19$ for non-calcareous, low total organic carbon mudstones.

Given porosity, we still need to know vertical effective stress to determine the β , and n_0 parameters in Eq. 3.4. We know the total vertical stress within the mudstone (Eq. 3.2) and must determine the pore pressure to determine vertical effective stress (Eq. 3.5). Our approach is to assume that the sandstone (black circle, **Fig. 3.7e, f**) excess pressure equals the excess pressure within the nearest mudstone sample above and below (red dots, **Fig. 3.7e, f**)

We constrained the parameters n_0 and β in Eq. 3.4 by taking a least squares regression of $\log(n)$ versus (σ'_v) . On a plot of vertical effective stress vs. porosity, the porosity at zero vertical effective stress is equal to n_0 and the slope is β . We used two approaches to constrain the parameters β and n_0 . In both cases, we used porosity and vertical effective stress measurements from well 826 #1. In method 1, we used every mudstone that had an adjacent sandstone pressure in the entire well (open and closed circles, **Fig. 3.8**), which included both Pleistocene and Miocene strata (dashed line, **Fig. 3.8**). In method 2, we used only the mudstones that had adjacent sandstone pressures within the Pleistocene strata (dash-dot line, **Fig. 3.8**).

The two different approaches result in substantially different compression parameters (**Fig. 3.8**). The porosity and effective stress relationship using all the mudstones (method 1) yielded a compressibility (β) of $1.24 \times 10^{-4} \text{ PSI}^{-1}$ ($1.8 \times 10^{-2} \text{ MPa}^{-1}$) and a reference porosity (n_0) of 0.303 (all circles, **Fig. 3.8**). In contrast, the Pleistocene strata (method 2) yielded a larger reference porosity (0.345 vs. 0.303) and a larger compressibility $1.79 \times 10^{-4} \text{ PSI}^{-1}$ ($2.6 \times 10^{-2} \text{ MPa}^{-1}$) vs. $1.24 \times 10^{-4} \text{ PSI}^{-1}$ ($1.8 \times 10^{-2} \text{ MPa}^{-1}$). As a

result, method 2, where the relationship is based only on the Pleistocene strata, predicts significantly lower effective stresses in the Miocene mudstones (**Fig. 3.8**)

In the Gulf of Mexico several other porosity and vertical effective stress relationships for Pleistocene mudstones have been documented (**Fig. 3.8**). In the Bullwinkle Basin (Green Canyon 65) a mudstone compressibility (β) of $2.5 \times 10^{-4} \text{ PSI}^{-1}$ ($3.62 \times 10^{-2} \text{ MPa}^{-1}$) and a reference porosity (n_0) of 0.40 were found (Flemings and Lupa, 2004). The Eugene Island 330 field documented a Pleistocene mudstone compressibility (β) of $2.54 \times 10^{-4} \text{ PSI}^{-1}$ ($3.68 \times 10^{-2} \text{ MPa}^{-1}$) and reference porosity (n_0) of 0.40 (Hart et al., 1995). These parameters are more in line with those found in the Pleistocene mudstone at Mad Dog (**Table 3.3**).

We next explore the mudstone pressure predictions of the two regression relationships. To do so, equations 3.4 and 3.5 are combined to predict fluid pressure (u):

$$u = \sigma_v - \left[\frac{1}{\beta} \ln \left(\frac{n_0}{n} \right) \right] \quad (\text{Eq. 3.7})$$

The right side of Eq. 3.7 will predict physically impossible negative vertical effective stresses for porosities $> n_0$. Therefore, the porosity intercepts for each regression can be substituted into Eq. 3.6 to back out maximum allowable transit times for effective stresses ≥ 0 . The limits are $147.7 \mu\text{s}/\text{ft}$ for the fit of all the data, and $169.2 \mu\text{s}/\text{ft}$ for the Pleistocene regression. Transit times greater than these will erroneously produce pore pressures greater than the total vertical stress.

3.5 MUDSTONE PRESSURE ACROSS MAD DOG

We used method 1 and method 2 to predict fluid pressures in 4 wells at Mad Dog (**Figs. 3.4, 3.5, 3.9, 3.10**). The two approaches yield very different mudstone pore pressures (red vs. gray dots, **Fig. 3.4e**) at the 826#1. Since the sonic data above 9000' are $> 147.7 \mu\text{s}/\text{ft}$, the regression based on all the data (method 1) results in predicted

mudstone pressures that are significantly above the total vertical stress in the shallow zone. In the deeper zone this approach predicts mudstone pressures that are less than the observed reservoir pressures (gray dots, **Fig. 3.4e**). In contrast the approach based only on the Pleistocene measurements (method 2) results in values that are less than but parallel to the total vertical stress in the shallow section but are greater than the reservoir pressures at depth (red dots, **Fig. 3.4e**).

In the shallow Pleistocene strata (7,000 to 11,000 ft), the difference between the two approaches is large, with much of the sonic data above the limit for non-negative effective stresses for the approach based on all the data (method 1) (**Fig. 3.4**). The porosity-vertical effective stress relationship from just the Pleistocene strata (method 2) suggests that excess pressure begins at 7,200 feet (2195 meters) and increases to approximately 8,000 feet (2438 meters). Shallow water flows were reported in this interval suggesting this section is, indeed, overpressured. Beneath 8,000 feet, predicted excess pressure is constant to approximately the base of the Pleistocene, paralleling the observed direct pressure measurements (open circles, **Fig. 3.4e**). In contrast, method 1, based on all the data, under predicts the deepest Pleistocene pressure measurements.

From the Pleistocene strata to the upper Miocene strata (15,500-16,700 feet, 4724-5090 meters), the predicted mudstone excess pressures rise and match the observed values using either calibration (**Fig. 3.4e**). Predicted excess pressures decline downward to the middle Miocene strata at 18,500 feet (5638 meters) with either method (**Fig. 3.4e**). The relationship based on all the data (method 1) predicts that mudstone pressures 383 psi (2.6 MPa, 0.4 ppg) less than the observed pore pressures within this interval whereas method 2 (based on the Pleistocene data) predicts the mudstone pressure 483 psi (3.3 MPa, 0.48 ppg) more than the observed pore pressure (**Fig. 3.4e**). Both approaches predict that pore pressure increases from the middle to lower Miocene strata, similar to

the direct pore pressure measurements. At the very base of the well the predicted pore pressure converged on measured values.

We next explore the predicted pressures for the 782 #1 well, the first subsalt well at Mad Dog. Method 1 and 2 predict pore pressures immediately beneath salt that are similar to the observed pressures (black dot, 15,500 ft, **Fig. 3.5e**). This zone has the lowest vertical effective stresses observed during drilling at Mad Dog beneath salt. Both method 1 and method 2 predict mudstone pressures that are greater than the observed pressures in the middle Miocene (**Fig. 3.5e**). This contrasts the prediction at the 826 #1, where method 1 predicted mudstone pressures below the measured pressures in the middle Miocene (compare Fig. 3.4 and Fig. 3.5). Similar, both methods predict an increase in mudstone pore pressures from the middle to lower Miocene strata.

Well 783 #1, penetrated 7,200 feet (2,195 meters) of salt and the subsalt sediments are Miocene in age (**Fig. 3.9**). There were no direct pressure measurements in the upper Miocene strata but the predicted mudstone excess pressure is large directly below salt (**Fig. 3.9e**). From the middle Miocene to the lower Miocene strata, the predicted mudstone pressure for the Pleistocene regression (method 2) is ~2,000 psi (13.8 MPa) more than the measured sandstone pressure (red vs. black dots). However, one pore pressure measurement immediately below the PQRS sandstone shows a significantly higher pressure (open circle, **Fig. 3.9e**). This measurement taken by the Modular Dynamic Formation Tester (MDT) tool is within 5 psi of the mud hydrostatic pressure. While this raises the possibility of supercharging or seal leakage, the test's drawdown mobility factor (206) is substantially higher than other, lower pressure tests. Consequently, we have not ruled out the possibility that this data point could in fact be valid. Finally, well 826 #5 in the southwest region of Mad Dog penetrated 2,700 feet (823 meters) of salt, where the salt approaches the seafloor (**Fig. 3.10**). The predicted

mudstone pressures for both regressions once again overestimate the direct measurements within the middle and lower Miocene strata.

3.6 DISCUSSION

The selection of a particular compression curve is one of the fundamental challenges of pore pressure prediction. We interpret that the compression curve that is calibrated by the Pleistocene pore pressure measurements (method 2) gives the most physically meaningful results for three reasons. First, the results successfully predict that shallow excess pressure that is present in the section and matches the direct measurements in both the Pleistocene and upper Miocene strata at 826#1 (**Fig. 3.4e**). Second, the compression parameters (n_0 and β) based on the Pleistocene strata are characteristic of other compression curves used in Gulf of Mexico mudstones. Lastly, the predicted mudstone pressures using method 1 (all direct pressure measurements) underestimates some of the middle Miocene sand pressures at the 826 #1 and 782 #1 wells (Fig. 3.8, 3.9), which seems physically unreasonable. A fundamental outcome of this approach is that the sandstones within the middle and lower Miocene strata have lower in-situ pressures than the bounding mudstone. In the ensuing analysis we assume that the porosity-vertical effective stress relationship in the Pleistocene strata (method 2) provides the most accurate prediction and we use it to analyze the variation between mudstone pressure and sandstone pressure in the Mad Dog field.

At Mad Dog, the difference between the sandstone pressure and the predicted mudstone pressure at a given stratigraphic horizon was significantly different in different wells. For example, the mudstone pore pressure predicted by method 2 in the 826 #1 well in the N sandstone is fairly small (within 600 psi and 0.28 ppg) (**Fig. 3.4**) of the sandstone pressure whereas at the same horizon in the 826 #5 well, the difference

between the pore pressure and the sandstone pressure is much greater (1,855 psi and 1.13 ppg) (**Fig. 3.10**). We find that this pressure difference increases with increasing vertical stress at all of the mapped horizons (**Fig. 3.11**).

To illuminate the relationship between mudstone pressure and total vertical stress, we explored how vertical effective stress in the mudstone is varying between the wells. The vertical effective stress (σ'_v) is calculated directly from porosity (Eq. 3.4), and the pore pressure is then calculated by subtracting the vertical effective stress from the total stress (Eq. 3.7). To understand how total vertical stress is impacting the pore pressure (**Fig. 3.11**), we need to understand how the vertical effective stress in the mudstone above each reservoir horizon is varying. In the N middle Miocene sandstone, we find that at all of the wells where this sand was penetrated, the velocities used to compute offset mudstone pore pressures lie within $\pm 1\%$ of their average value (**Fig. 3.12**). In fact, the mudstones bounding every regional aquifer that we mapped (N, PQRS, V, and the DD, EE, and FF) all show the similar behavior. The velocity picks for the PQRS and DD, EE, FF mudstones fall with $\pm 4\%$ of their average, while the range for the V mudstones is $\pm 2\%$. Since the mudstone velocities adjacent to each sand fall within a narrow range, the same holds true for porosity and vertical effective stress (**Table 3.4**).

If we take the derivative of equation 3.5 and assume that the vertical effective stress is constant in the mudstone as observed, we find that any change in pore pressure must be equal to any change in vertical stress:

$$du = d\sigma_v. \quad (\text{Eq. 3.8})$$

Thus, if the vertical effective stress in the mudstone is constant, then a plot of the mudstone pressure vs. the total vertical stress should vary in a one to one fashion. We show that at the four mapped sandstone bodies, the predicted mudstone excess pressure does increase linearly with total vertical stress (**Fig. 3.13**). The sandstone excess

pressures appear as a vertical line and the mudstone excess pressures increase and nearly parallel the total stress less the hydrostatic pressure ($\sigma_v - u_h$) curve in all the Miocene strata (**Table 3.5**). For each sandstone mapped, there is a linear increase in the mudstone excess pressure with stress, whereas the sandstone excess pressure is constant because it lies along the hydrostatic gradient. The slopes of $du^*/d(\sigma_v - u_h)$ range from 0.55 to 1.36 (**Table 3.5**) with two of the four slopes being greater than 1.0. If the slope is less than 1.0, then the pore pressure is rising less than the total vertical stress. If the slope is greater than 1.0, then the pore pressure is rising more than the total vertical stress.

The brown dashed lines in Fig. 3.13, drawn parallel to the $\sigma_v - u_h$ curves (solid brown lines) show an alternative fit of the data, in which $u^* = (\sigma_v - u_h) - \sigma'_{\text{avg}}$, and σ'_{avg} is the average vertical effective stress for each mudstone group. The fit of the data is nearly as good as the linear regressions. Consequently, this suggests a simple way to extrapolate pore pressures in the bounding mudstones for each Miocene sand from one location to another, as will be discussed below.

This has led us to a conceptual understanding that the mudstones pressures near the bounding reservoir vary linearly with the total vertical stress across the Mad Dog field (**Fig. 3.14**). For example, the well 826 #1, drilled in the deepest water outboard of the Sigsbee Escarpment has the lowest mudstone pore pressure because it has the lowest total vertical stress. In contrast, the 826 # 5, which is both beneath the Sigsbee Escarpment and in a down dropped graben, has the largest total vertical stress and hence the highest pore pressure. We infer a linear variation in the mudstone pressure across the structure, suggesting if low on the structure, the pore pressure will become greater as a result of the increase in total vertical stress. In summary, not only are the mudstone pressures different from the reservoir pressure at Mad Dog, the difference in these pressures varies

significantly with total vertical stress and this can be systematically predicted based on total vertical stress.

The interpretation that the vertical effective stress in the mudstone can be approximated as constant implies a means to predict mudstone pore pressure in a new drilling location given an initial, offset, well. Specifically, the mudstone pressure can be predicted from the vertical stress at the new well and the vertical effective stress encountered at the old (offset) well.

$$u_{mudstone} = \sigma_v - \sigma'_{v_{offset\ well}}. \quad (\text{Eq. 3.9})$$

Similarly, given that the excess pressure in the connected permeable sandstone bodies is constant, the sandstone pore pressure can be predicted by adding the hydrostatic pressure in the new well to the excess pressures in the offset well:

$$u_{sandstone} = u^* + u_h. \quad (\text{Eq. 3.10})$$

It is now fairly routine to build three dimensional total vertical stress models that account for the spatial variation in stress. Thus, it is a fairly simple step to use Equations 3.9 and 3.10 to predict mudstone and sandstone pressures across fields such as Mad Dog.

The observation that estimated mudstone pressures do not match observed reservoir pressures is a well-recognized challenge in pore pressure prediction. Flemings et al. (2002) documented this behavior in the EI-330 field. Flemings and Lupa (2004) explored the variation in pressures in mudstones bounding the J sandstone reservoir and showed that they co-varied in a very similar fashion at Bullwinkle. High on the structure (where total vertical stress is less), the mudstone pressure is less whereas deep on the structure, where total vertical stress is more, mudstone pore pressure is greater and follows the total vertical stress gradient. The challenge at Mad Dog is that because of the presence of thick salt and significant changes in total vertical stress thickness, a simple plot of pressure vs. depth does not show as clearly the relationship shown in Fig. 3.13. In

fact, Appendix E shows significantly less correlation when depth vs. pressure is plotted as opposed to stress.

In this study, we chose a pore pressure prediction method that was based on pressure measurements made in Pleistocene strata (method 2, Fig. 3.8). It is very important to recognize that regardless of whether method 2, method 1, or a different calibration measurement was used, we would observe the same spatial variation on mudstone pore pressure (e.g. Figs. 3.13 and 3.14). This is because the key observation is that the velocity and hence the porosity and the vertical effective stress can be approximated as constant in mudstones bounding particular reservoirs. We emphasize this because there is inevitable debate over which calibration approach is most appropriate in pore pressure prediction.

The recognition that mudstone and sandstone pore pressures are different at a particular horizon should play an important role in well design. At Mad Dog, sandstone pressures are generally below mudstone pressures (e.g. Fig. 3.10). Borehole pressure must stay above the pore pressure in the permeable sandstones. However, if the borehole pressure is only raised to the value necessary to exceed the sandstone pressure, it will be significantly lower than the mudstone pressure. This increases the risk that there will be compressive collapse of the wellbore in the mudstone interval and stuck pipe (French and McLean, 1993; Luo et al., 2012b). In addition, if we encounter localized sandstones with pore pressures equal to the mudstone pressure, then pressure kicks may occur. In contrast, if the borehole pressure is raised to equal the mudstone pressure, the borehole pressure will exceed the sandstone pressure significantly, which increases the risk of fracturing the sand, and therefore, drilling fluid losses. Since the sandstone and mudstone pressures vary, the fracture gradient also varies. Thus, changes in the fracture gradient should also be accounted for when penetrating sandstones vs. mudstones. At Mad Dog, the difference

between mudstone pore pressure and sandstone pore pressure increases with total vertical stress. This suggests that the more challenging wells will be the wells drilled where the total vertical stress is greatest. Finally, in subsalt fields with significant bathymetry, such as Mad Dog the spatial variation in total vertical stress must be calculated to successfully predict pore pressure.

3.7 CONCLUSIONS

We have performed a pore pressure analysis of the of the Mad Dog field in the deep-water Gulf of Mexico. We show the following.

- 1) The mudstone pressure is predicted from its porosity with an exponential porosity vs. vertical effective stress relationship where porosity is interpreted from wireline velocity. We find a porosity-effective stress relationship based on pore pressure measurements made in Pleistocene sediments to most accurately predict the subsurface mudstone pressure.
- 2) At Mad Dog, extraordinary lateral changes in total vertical stress due to changing bathymetry and the presence/absence of salt must be accounted for to successfully predict pressure.
- 3) Mudstones bounding regional, hydraulically connected, sandstones have a constant porosity throughout the field from which we interpret the vertical effective stress can be approximated as constant. As a result, mudstone pore pressures can be extrapolated along the total vertical stress gradient whereas sandstone pressures follow the hydrostatic gradient in Miocene strata.
- 4) We find that the difference between the mudstone pressure and the sandstone pressure is proportional to the total vertical stress and we show that the pore pressures within mudstones can be systematically different

from that of the nearby sandstones and that this difference can be predicted. Well programs must ensure that the borehole pressure is not too low, which results in tight hole and stuck pipe in the mudstone intervals, and not too high, which can result in lost circulation to the reservoir horizons.

3.8 FIGURES

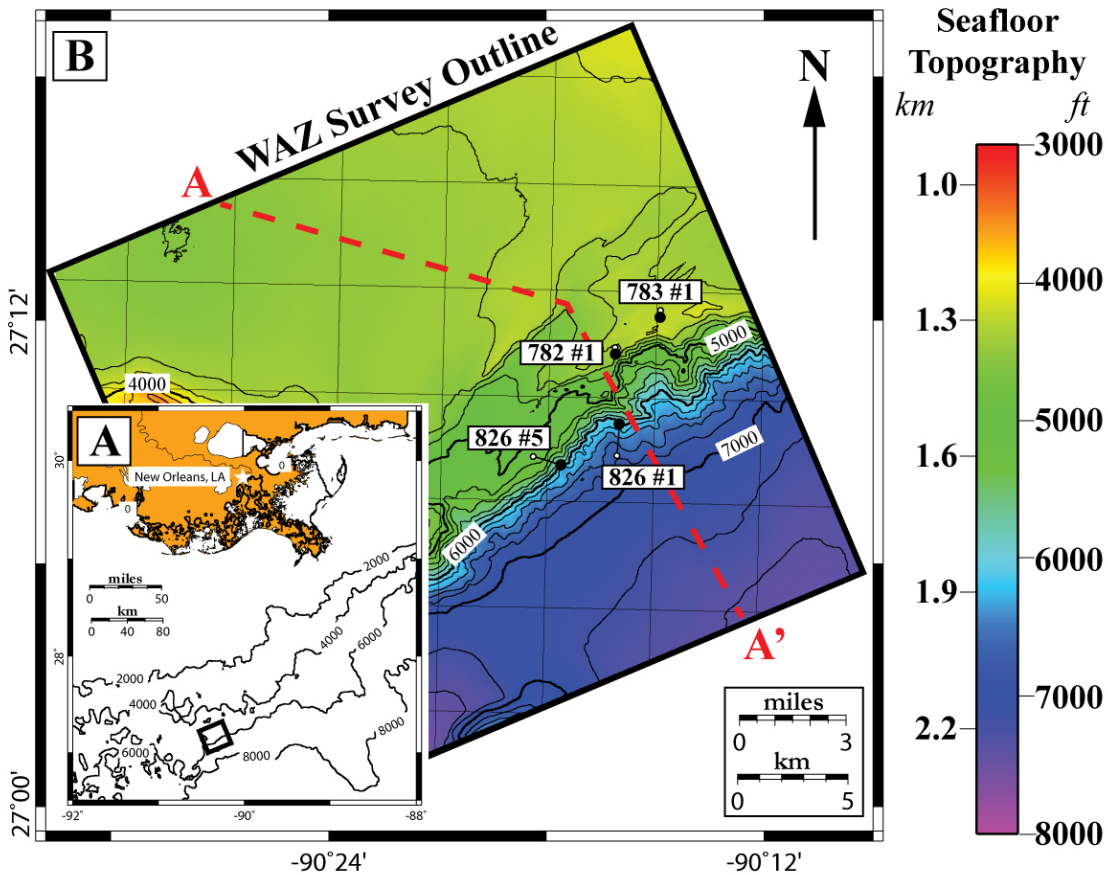


Figure 3.1: Location and base map of the Mad Dog field, Gulf of Mexico

(A) The Mad Dog field (black box) located approximately 190 miles southwest (306 kilometers) of New Orleans. The seafloor topography illustrated with 2000 feet contours from NOAA bathymetry data. (B) The black outline represents the 3D wide azimuth seismic survey (WAZ). The seafloor bathymetry is illustrated with 200 feet contours from the WAZ survey. Note the large change in bathymetry between well 826 #1 outboard of the Sigsbee escarpment and the 3 wells (826 #6, 783 #1, and 782 #1) inboard of the Sigsbee Escarpment. Well 826 #1 is outboard of salt and was used to determine the porosity and vertical effective stress relationship at Mad Dog. The other noted wells are used to predict pore pressure on from the porosity and vertical effective stress relationship. The open white circles represent the surface well locations and the black circles represent the bottom hole locations. Cross A-A' is shown in Figure 3.2.

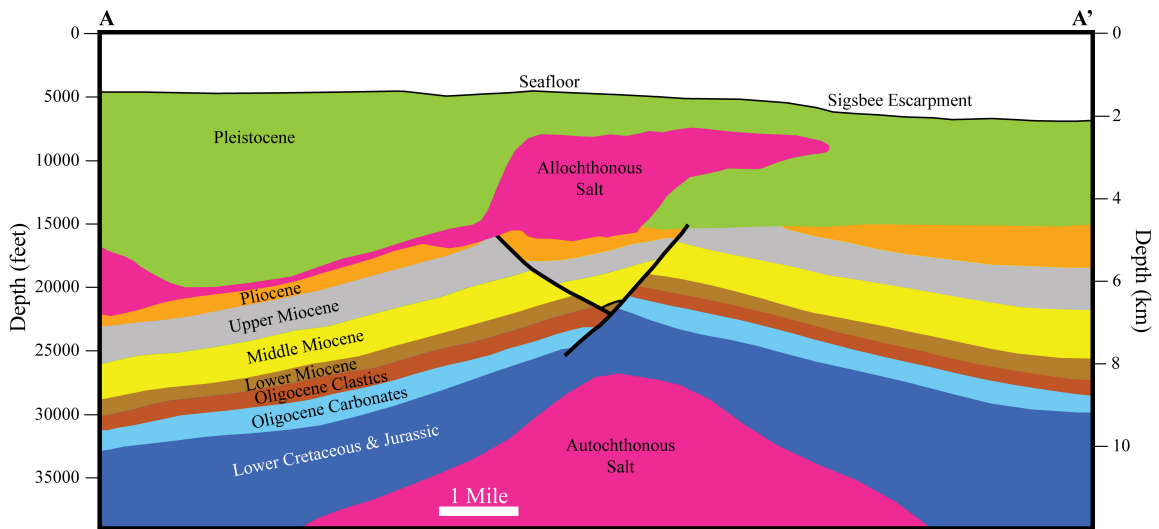


Figure 3.2: Geologic cross section through the Mad Dog field

Cross section illustrates the salt distribution and the regional stratigraphy. The Mad Dog field is a faulted anticline with production predominately from the lower Miocene sandstones. Oil and gas is also present in the upper Miocene and produced from one well. Cross section A-A' location is shown in Figure 3.1. Figure modified from BP.

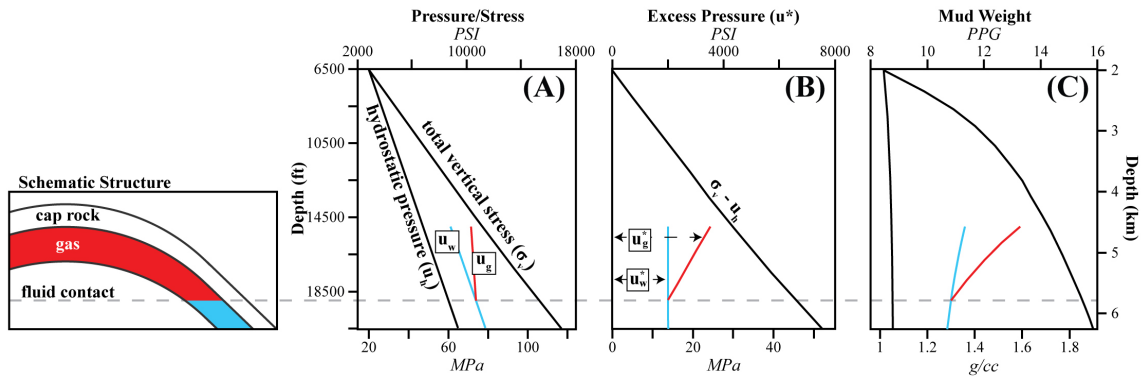


Figure 3.3: Schematic diagram of a sandstone with multiple fluids present and the associated pressures

The schematic diagram shows a sandstone with water and gas present with a fluid contact indicated (gray dashed line). The total vertical stress (σ_v) was calculated by integrating a bulk density log with depth. The excess pressure (u^*) was calculated by subtracting the absolute pressures/stresses from the integration of a constant water density of 1.023 g/cc (0.44 psi/ft) from the seafloor to the total depth. The associated water phase (u_w) and gas phase (u_g) pressures are shown in pressure/stress (a), excess pressure (b), and mud weight (c) space. The pressure within the oil/gas phases around the Mad Dog field are converted to the aquifer phase pressure when the fluid contact is known.

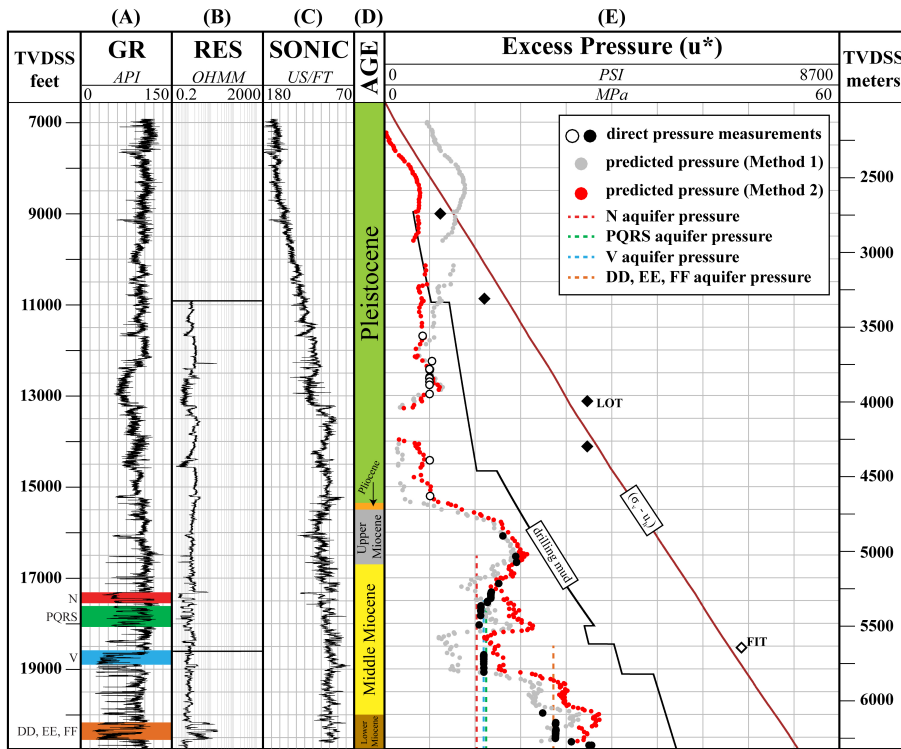


Figure 3.4: Pressure versus depth plot of the discovery well 826 #1

The wireline gamma ray, resistivity, and sonic logs (a-c) and the associated pressure and stress from the discovery well 826 #1 plotted in excess pressure (e) space. The excess pressure (u^*) was calculated by subtracting the absolute pressures/stresses from the integration of a constant water density of 1.023 g/cc (0.44 psi/ft) from the seafloor to the total depth. The total vertical stress was calculated by integrating the bulk density log with depth. The predicted pore pressure (red circles) using the Pleistocene direct pressure measurements (open circles, method 2) for porosity-effective stress calibration provides an accurate pressure prediction in the Pleistocene and overestimates pressure in the Miocene strata. The predicted pore pressure (gray circles) using all the direct pressure measurements (open/black circles, method 1) for porosity-effective stress calibration does not predict accurate shallow pressures (intersects σ_v), under predicts pressure in the middle Miocene strata, and overestimates pressure in the lower Miocene strata. The average sandstone excess pressures are shown as vertical dashed lines and colored accordingly (see Table 3.2). TVDSS = True Vertical Depth Subsea, FIT = Formation Integrity Test, LOT = Leak-Off Test.

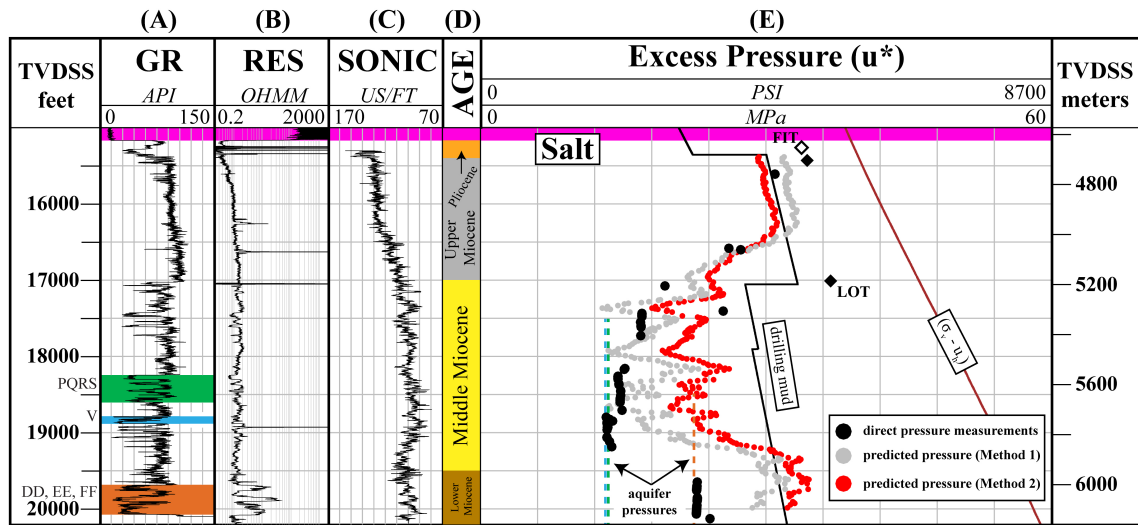


Figure 3.5: Pressure versus depth plot of the first appraisal well 782 #1

The wireline gamma ray, resistivity, and sonic logs (a-c) and the associated pressure and stress from the 1st appraisal well 782 #1 plotted in excess pressure (e) space. Well 782 #1 penetrated 5,000 feet (1,524 meters) of salt. The predicted pore pressure using method 2 (red circles) matches direct pore pressure measurements (black circles) directly below salt except in the middle and lower Miocene strata where the prediction is over estimated. The predicted pressure using method 1 (all direct pressure measurements from well 826 #1) is shown with gray circles. The average sandstone excess pressures are shown as vertical dashed lines and colored accordingly (see Table 3.2).

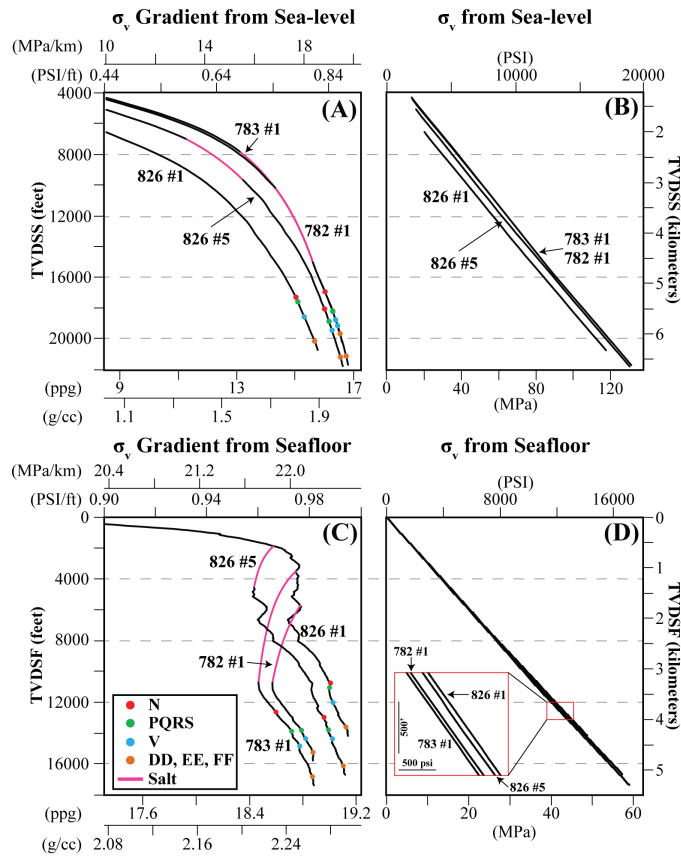


Figure 3.6: Total vertical stress gradients and total vertical stress from sea-level and seafloor

(A) The total vertical stress gradient from sea-level for the 4 wells at Mad Dog. The salt gradient is plotted (pink line) where a constant density of 2.2 g/cc was used (Balk, 1949, 1953; Hudec et al., 2009; Lerche and Petersen, 1995; Nance et al., 1979; Nance and Wilcox, 1979). Well 826 #1 has the smallest gradient because of the topography at Mad Dog where well 782 #1 has a water depth of 4,423 feet (1,348 meters) and 826 #1 at 6,560 feet (2,000 meters). (B) The total vertical stress from sea-level. (C) The total stress gradient from the seafloor. This plot removes the water depth/ topography affect. The increasing salt thickness in wells 826 #5, 782 #1, and 783 #1 causes the total vertical stress gradient to decrease compared to the outboard of salt well 826 #1. (D) The total vertical stress from the seafloor. Note the shift of well 826 #1 from plot (A,B) to (C,D). This is a direct result of the large topography contrast between 826 #1 and the other wells.

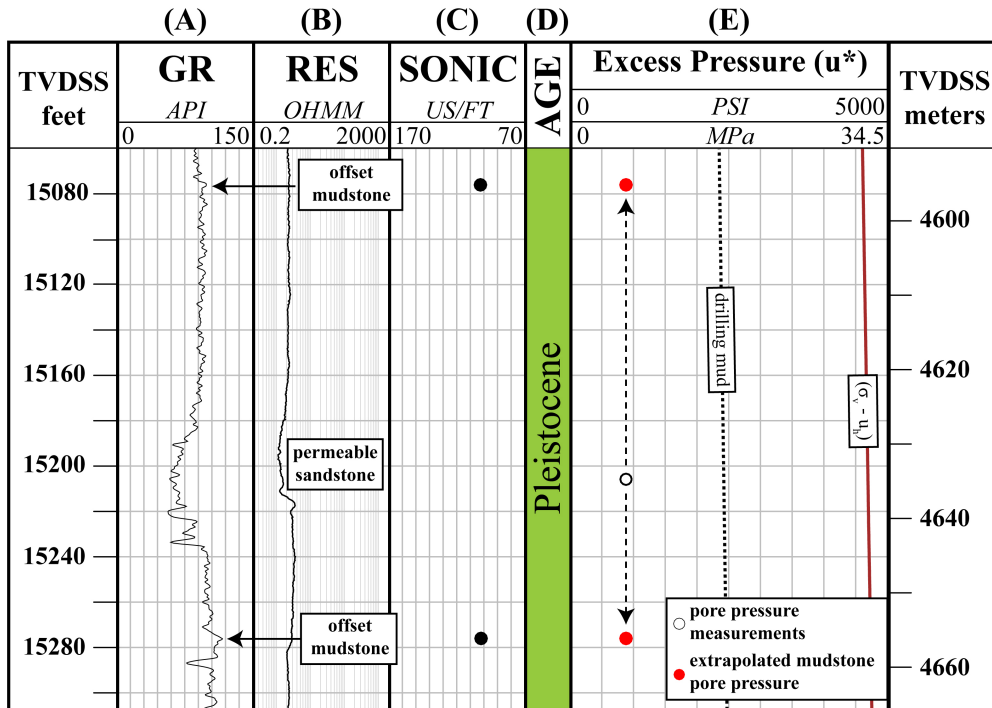


Figure 3.7: Example of relating direct pore pressure in sandstone to the offset mudstone for porosity and vertical effective stress calibration in well 826 #1

The gamma ray and resistivity logs (a, b) indicates the permeable sand and offset mudstone strata. The sonic values (c) in the offset mudstone are shown (black circles) and the porosity (n) is calculated from Equation 3.6. The measured pressure in sand (open circle, e) is extrapolated along the formation water gradient to the offset mudstone above and below (red circles, e) the measured pressure. This assumes the sandstones and mudstones are in pressure equilibrium. The extrapolated pore pressure is subtracted from the total vertical stress (σ_v) to give the vertical effective stress (σ'_v) in the mudstone. This method is applied to the direct pressure measurements in well 826 #1 to calculate a porosity-vertical effective stress relationship in mudstones.

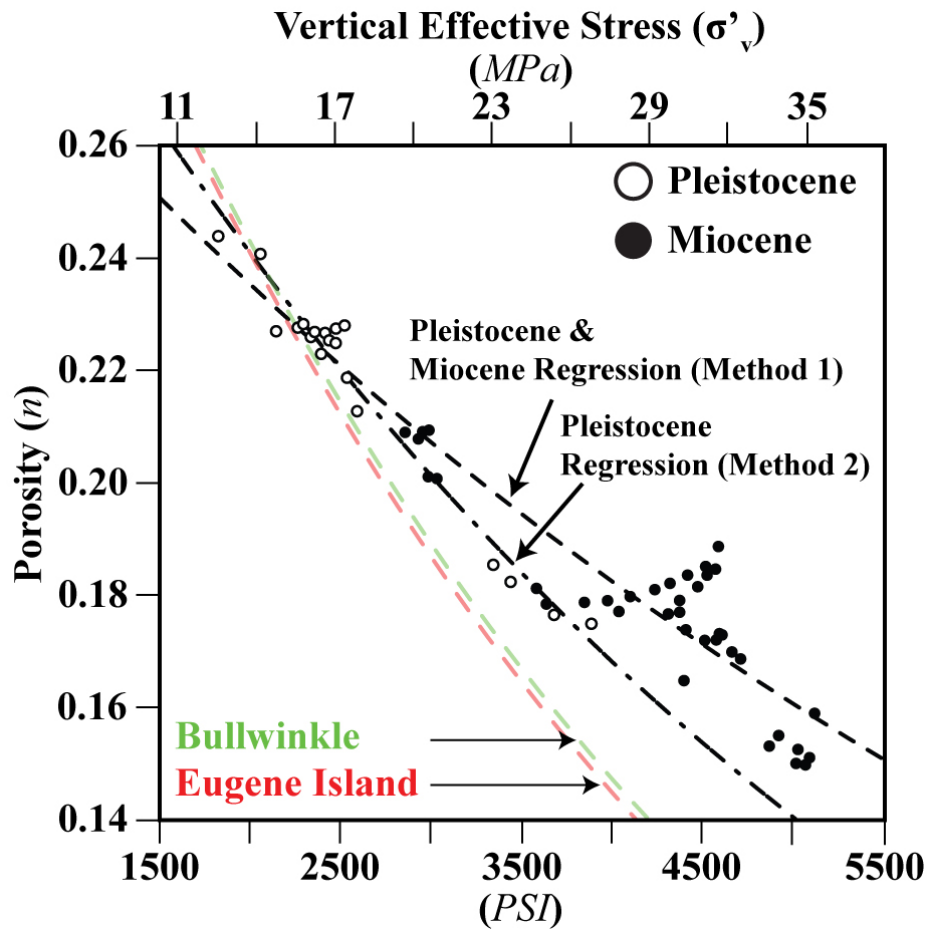


Figure 3.8: Mudstone porosity versus vertical effective stress in well 826 #1

The porosity and vertical effective stress relationship in mudstone using all the direct pressure measurements (all circles, method 1) (see Fig. 3.4). The mudstone porosity and vertical effective stress relationship yields a compressibility (β) of $1.24 \times 10^{-4} \text{ PSI}^{-1}$ ($1.8 \times 10^{-2} \text{ MPa}^{-1}$) and a reference porosity (n_0) of 0.303 from the linear regression (dashed line). The porosity and vertical effective stress relationship in Pleistocene mudstone (open circles) from the direct pressure measurements (method 2) (see Fig. 3.4). The mudstone porosity and vertical effective stress relationship yields a compressibility (β) of $1.79 \times 10^{-4} \text{ PSI}^{-1}$ ($2.6 \times 10^{-2} \text{ MPa}^{-1}$) and a reference porosity (n_0) of 0.345 from the linear regression (dashed/dot line). The porosity-vertical effective stress calibrations from Bullwinkle and Eugene Island are shown. Note the reference porosity (y-intercept) is at 0.0 vertical effective stress. A summary of the reference porosity and compressibility is found in Table 3.3.

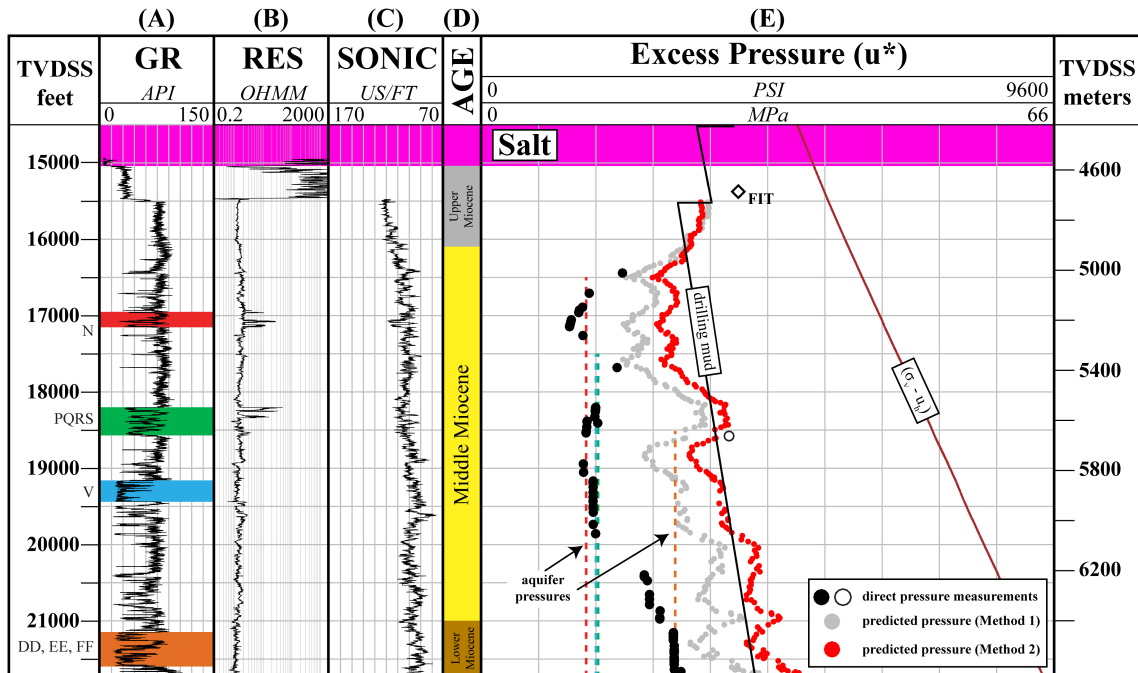


Figure 3.9: Pressure versus depth plot of well 783 #1

The wireline gamma ray, resistivity, and sonic logs (a-c) and the associated pressure and stress for well 783 #1 plotted in excess pressure (e) space. Well 783 #1 penetrated 7,200 feet (2,195 meters) of salt. The predicted pore pressure using method 2 (red circles) over estimate the direct pore pressure measurements (black circles) in the middle and lower Miocene strata. The predicted pore pressure suggests a high overpressure directly below salt. There is one direct pressure measurement (open circle) within the middle Miocene strata that is above the regional pressure trend at 12 ppg, which is in agreement with the predicted pore pressure for method 2 (Pleistocene regression). This measurement could reflect supercharging or seal leakage, and therefore, not be an accurate record of the in situ pore pressure. However, the test has a high mobility factor relative to some of the other tests, so the validity of this data point has not been completely ruled out. The predicted pressure using method 1 (all direct pressure measurements from well 826 #1) is shown with gray circles. The average sandstone excess pressures are shown as vertical dashed lines and colored accordingly (see Table 3.2).

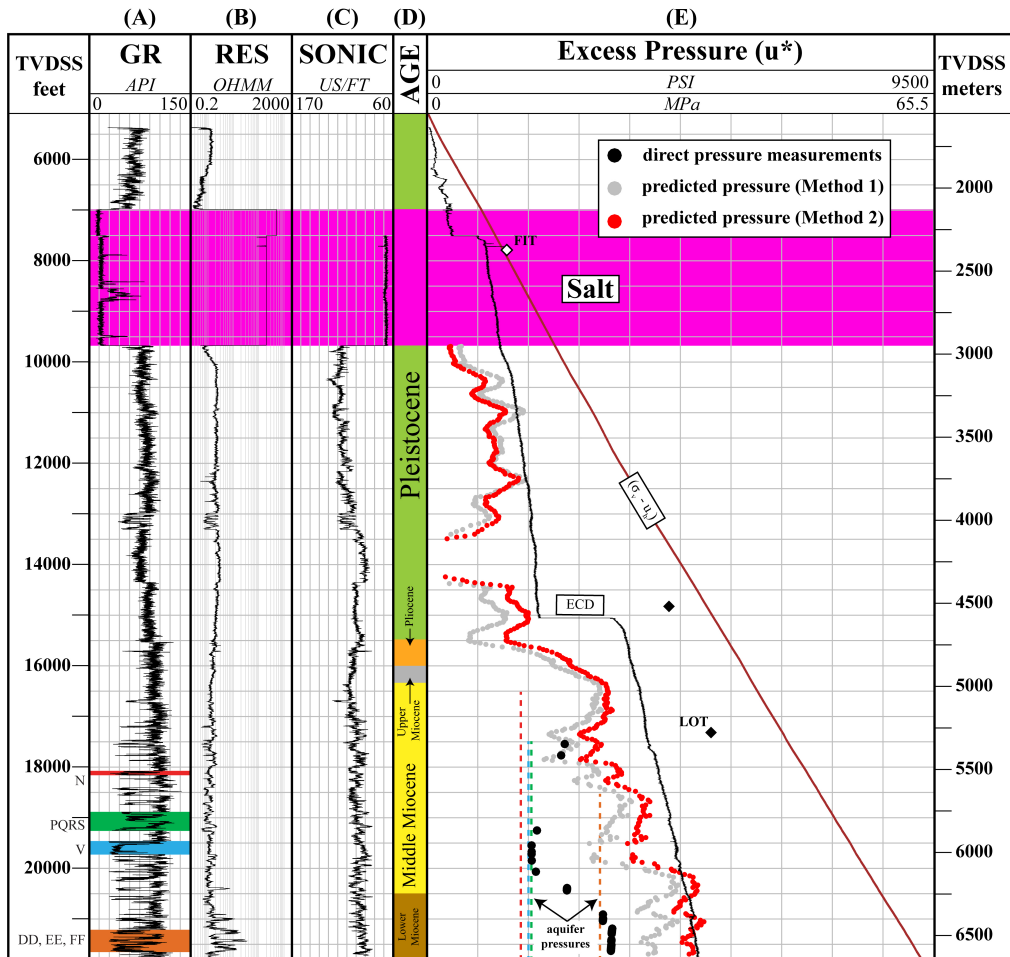


Figure 3.10: Pressure versus depth plot of well 826 #5

The wireline gamma ray, resistivity, and sonic logs (a-c) and the associated pressure and stress from well 826 #5 plotted in excess pressures (e) space. Well 826 #5 penetrated 2,700 feet (823 meters) of salt near the seafloor. There were no direct pressure measurements (black circles) near the base of salt but the predicted pore pressure using method 2 (red circles) suggest minimal overpressure. The predicted pore pressure suggests a large pressure increase from the Pleistocene to the upper Miocene strata. The predicted pore pressure substantially overestimates the direct pressure measurements in the middle and lower Miocene strata. The predicted pressure using method 1 (all direct pressure measurements from well 826 #1) is shown with gray circles. The average sandstone excess pressures are shown as vertical dashed lines and colored accordingly (see Table 3.2). ECD = Equivalent Circulating Density.

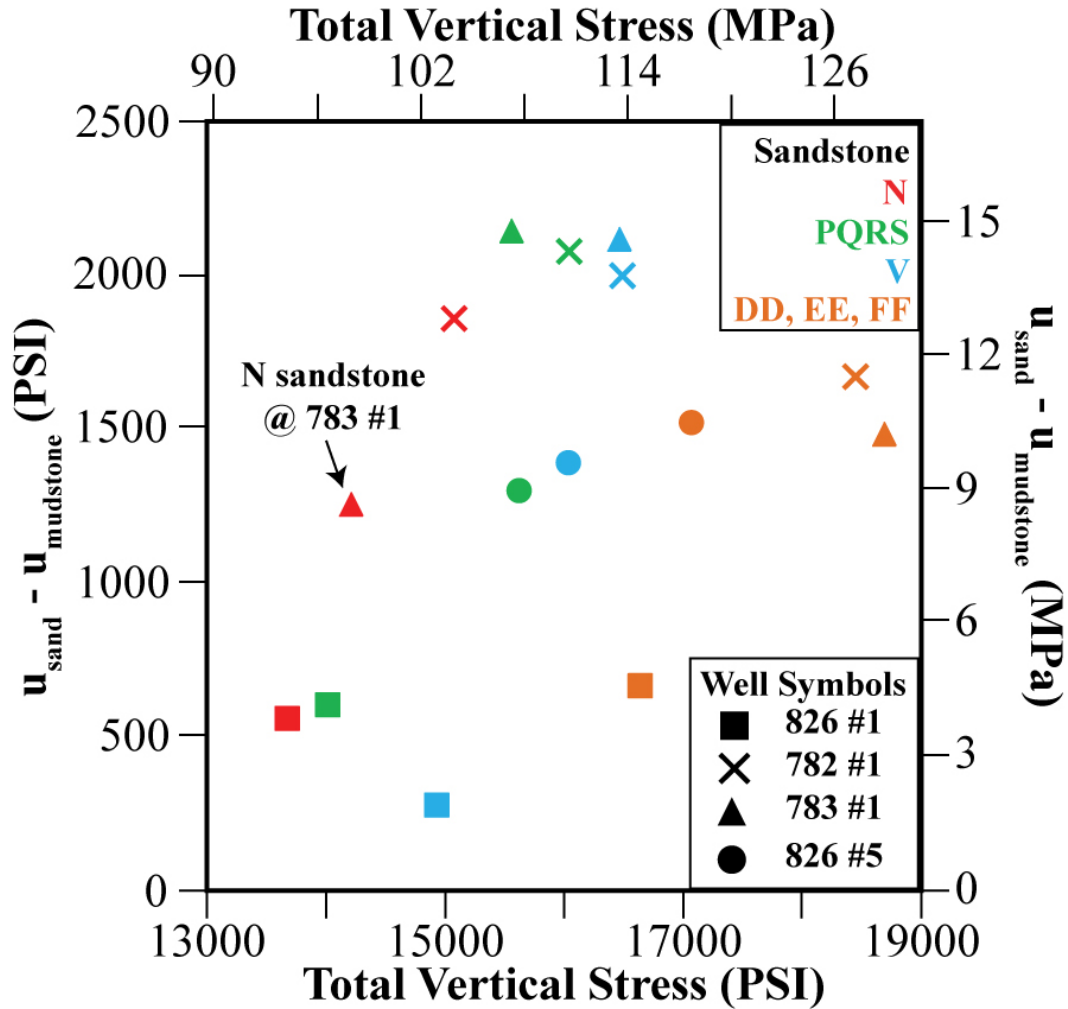


Figure 3.11: Difference between sandstone and mudstone pressures in the middle and lower Miocene

The difference between the predicted and measured pressures and total vertical stress are plotted in pressure space. Mudstone pore pressures were computed using the Pleistocene porosity-vertical effective stress relation (method 2). The various colors represent the individual sandstones (N, PQRS, V, and DD, EE, and FF) and the symbols represent the well locations (826 #1, 782 #1, 783 #1, 826 #5). In general, the larger the total vertical stress the larger the difference between the predicted mudstone pressure and the measured sandstone pressure.

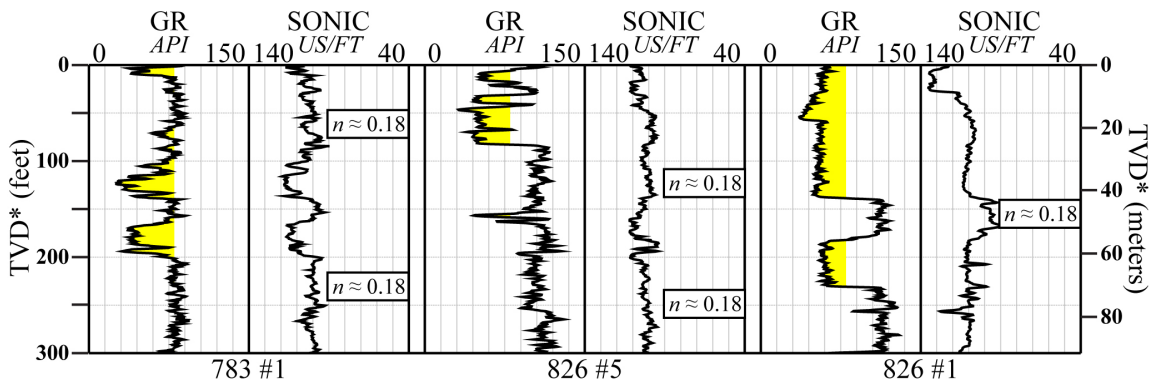


Figure 3.12: Constant mudstone porosity near the N sandstone

The gamma and sonic logs for wells 783 #1, 826 #5, and 826 #1 are shown and hung from the top of the N middle Miocene sandstone (yellow). The sonic values within the mudstone have more or less the same values between all three wells. This infers that the calculated porosity (n) through Equation 3.6 from the sonic log will have the same porosity. The mudstone thickness and stratigraphic location varies between the wells but the porosity is constant. Note: TVD* equals True Vertical Depth below top of N sandstone.

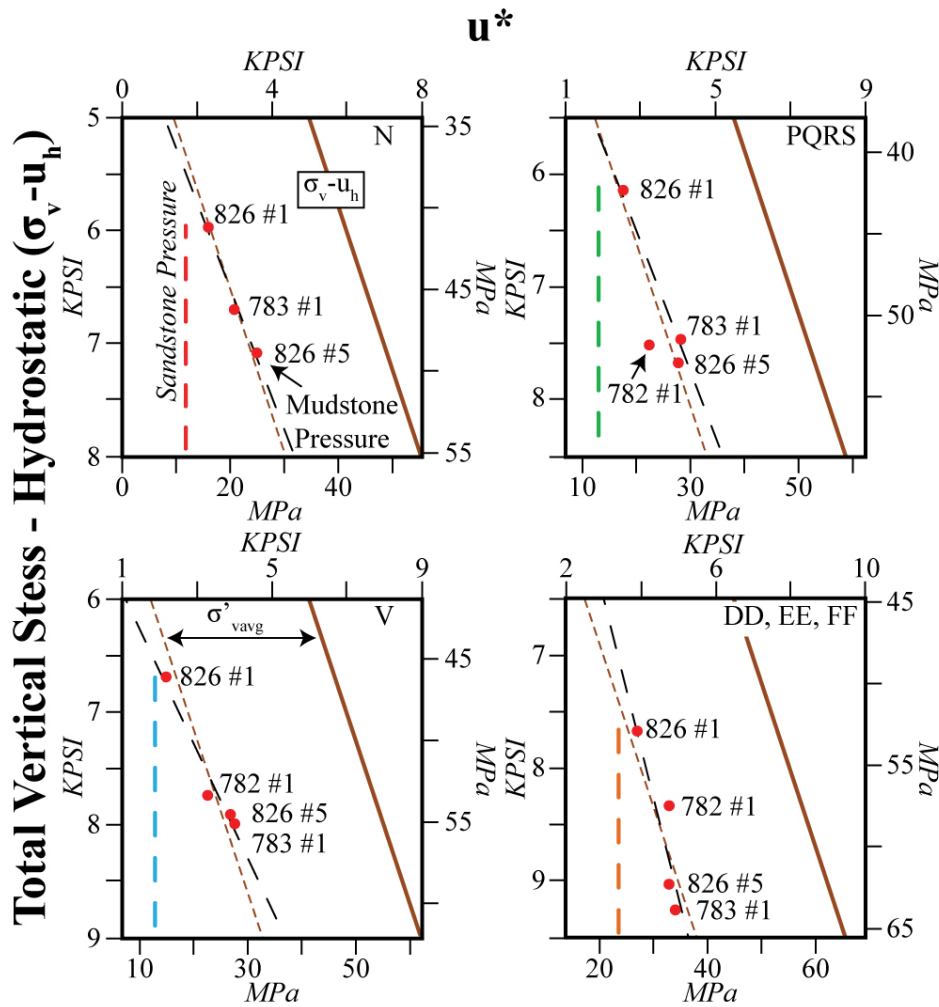


Figure 3.13: Sandstone and mudstone pressures across the field

The total vertical stress (σ_v) less the hydrostatic pressure (u_h) is plotted against excess pressure (u^*). The sandstone excess pressures (black lines) appear as a vertical line and the mudstone excess pressures (red circles) increase with increasing $\sigma_v - u_h$. A regression is taken through the mudstone excess pressures (dashed black line) which indicates u^* increases linearly with $\sigma_v - u_h$. The brown dashed line, drawn parallel to the $\sigma_v - u_h$ curve (solid brown line) shows an alternative fit of the data, in which $u^* = (\sigma_v - u_h) - \sigma'_{\text{avg}}$, and σ'_{avg} is the average vertical effective stress for each group (Table 3.4). The sandstone excess pressures are extrapolated to the lowest known excess pressure at Mad Dog. Table 3.5 summarizes the slope, y-intercept, R^2 , and $\sigma_v - u_h$ at the projected intersection of the sandstone and mudstone excess pressures.

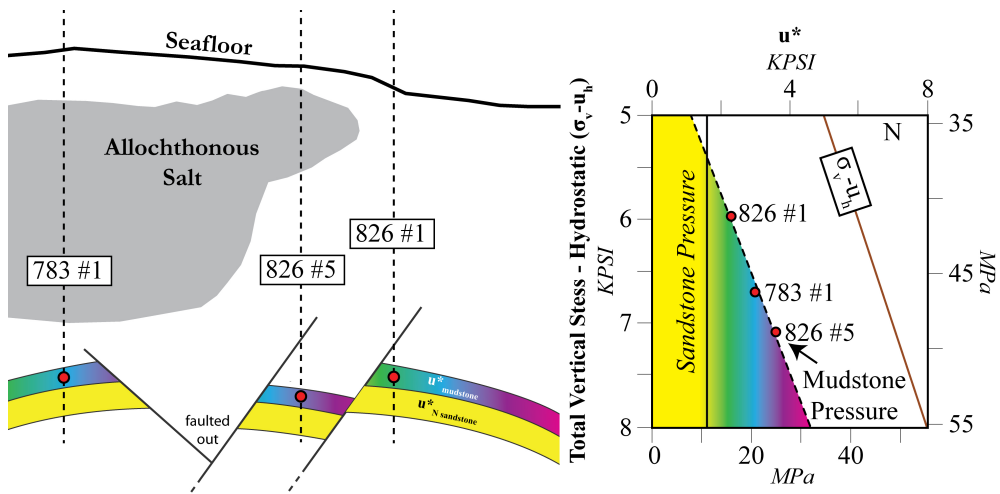


Figure 3.14: Schematic sandstone and mudstone pressure below salt

A conceptual model of how the mudstone pressures near the bounding sandstone reservoir co-vary with the total vertical stress across the Mad Dog field. The sandstone excess pressures remain constant across the field (yellow). The 826 #1 drilled outboard of salt has the lowest total stress, thus the excess pressure in the mudstone will have the lowest excess pressure (u^*). As the total vertical stress increases inboard of salt, the excess pressure is larger in the mudstone.

3.9 TABLES

Symbol	Name	Dimensions	Units
z	Depth	L^1	<i>feet or meters</i>
TVDSS	true vertical depth subsea (sea-level)	L^1	<i>feet or meters</i>
TVDSF	true vertical depth below seafloor	L^1	<i>feet or meters</i>
σ_v'	vertical effective stress	$M^1L^{-1}T^{-2}$	<i>PSI or MPa</i>
σ_v	total vertical stress	$M^1L^{-1}T^{-2}$	<i>PSI or MPa</i>
u	pore pressure	$M^1L^{-1}T^{-2}$	<i>PSI or MPa</i>
u^*	excess pressure	$M^1L^{-1}T^{-2}$	<i>PSI or MPa</i>
u_h	hydrostatic pore pressure	$M^1L^{-1}T^{-2}$	<i>PSI or MPa</i>
n	Porosity	-	-
n_0	reference porosity	-	-
ρ	bulk density	M^1L^{-3}	<i>lbs/ft³ or g/cm³</i>
Δt_{ma}	matrix travel time	$L^{-1}T^1$	<i>μs/ft or μs/m</i>
Δt	log-derived travel time	$L^{-1}T^1$	<i>μs/ft or μs/m</i>
x	acoustic formation factor	-	-
β	compression coefficient	$M^{-1}L^1T^2$	<i>PSI⁻¹ or MPa⁻¹</i>
g	acceleration of gravity	L^1T^{-2}	<i>ft/s² or m/s²</i>
FIT	formation integrity test	$M^1L^{-1}T^{-2}$	<i>PSI or MPa</i>
LOT	leak-off test	$M^1L^{-1}T^{-2}$	<i>PSI or MPa</i>
MDT	modular dynamic formation tester	$M^1L^{-1}T^{-2}$	<i>PSI or MPa</i>
ECD	equivalent circulating density	$M^1L^{-1}T^{-2}$	<i>PSI or MPa</i>
EMW	equivalent mud weight	M^1L^{-3}	<i>PSI/ft, MPa/km, lbs/gal (ppg), g/cm³</i>

Table 3.1: Nomenclature

$M = \text{Mass}$, $L = \text{Length}$, and $T = \text{Time}$.

Sand	Top depth below sea-level		Top depth below seafloor		u* sand				u* sand average	
	feet	meters	feet	meters	Min		Max		PSI	MPa
					PSI	MPa	PSI	MPa		
N	16500	5029	10926	3330	1480	10.2	2029	14.0	1755	12.1
PQRS	17500	5334	11314	3449	1758	12.1	2140	14.8	1949	13.4
V	17500	5334	12161	3707	1875	12.9	1935	13.3	1905	13.1
DD, EE, FF	18500	5639	13830	4215	3290	22.7	3200	22.1	3245	22.4

Table 3.2: Sandstone depth below sea-level, depth below seafloor, minimum and maximum excess pressure (u*), and average excess pressures (u*) values

Appendix D presents the details of the pore pressure analysis. Note: the average excess pressure values are used as reference for the sandstone excess pressures throughout this chapter.

Location	Strata	Compressibility (β)		Reference Porosity (n_0)
		PSI^{-1}	MPa^{-1}	<i>Unitless</i>
Mad Dog	Pleistocene & Miocene	1.24×10^{-4}	1.8×10^{-2}	0.303
Mad Dog	Pleistocene	1.79×10^{-4}	2.6×10^{-2}	0.345
Bullwinkle Basin	Pleistocene	2.5×10^{-4}	3.62×10^{-2}	0.40
Eugene Island	Pleistocene	2.54×10^{-4}	3.68×10^{-2}	0.40

Table 3.3: Compressibility and reference porosity for Mad Dog and other regions

The compressibility (β) and reference porosity (n_0) in Eq. 3.4 are constrained by taking a least squares regression of $\log(n)$ versus (σ'_v) .

Sand	Well	TVDSS		Depth Below Seafloor		Porosity	Transit Time		Velocity		Vertical Effective Stress		Avg. Vertical Effective Stress		Total Vertical Stress	
		feet	meter	feet	meter		%	$\mu\text{s}/\text{ft}$	$\mu\text{s}/\text{m}$	ft/sec	m/sec	PSI	MPa	PSI	MPa	PSI
N	826 #1	17486	5330	10926	3330	0.178	103	338	9716	2961	3666	25.3	3615	24.9	13669	94.2
	783 #1	17049	5197	12732	3881	0.179	103	339	9690	2954	3698	25.5			14206	97.9
	826 #5	18145	5531	13053	3979	0.184	105	343	9562	2914	3480	24.0			15074	103.9
PQRS	826 #1	17874	5448	11314	3449	0.179	103	339	9690	2954	3600	24.8	3727	25.7	14012	96.6
	782 #1	18413	5612	13990	4264	0.161	98	323	10162	3097	4274	29.5			15621	107.7
	783 #1	18376	5601	14059	4285	0.186	105	345	9510	2899	3380	23.3			15555	107.3
	826 #5	19014	5795	13922	4243	0.180	103	339	9664	2946	3654	25.2			16043	110.6
V	826 #1	18721	5706	12161	3707	0.153	96	316	10375	3162	4515	31.1	4239	29.2	14929	102.9
	782 #1	18848	5745	14425	4397	0.156	97	319	10295	3138	4451	30.7			16036	110.6
	783 #1	19245	5866	14928	4550	0.169	100	330	9951	3033	3977	27.4			16464	113.5
	826 #5	19494	5942	14402	4390	0.166	100	327	10029	3057	4014	27.7			16491	113.7
DD, EE, FF	826 #1	20390	6215	13830	4215	0.175	102	335	9794	2985	3767	26.0	3999	27.6	16644	114.8
	782 #1	19854	6051	15431	4703	0.183	104	342	9587	2922	3574	24.6			17072	117.7
	783 #1	21441	6535	17124	5219	0.164	99	325	10082	3073	4306	29.7			18465	127.3
	826 #5	21415	6527	16323	4975	0.152	96	315	10402	3170	4349	30.0			18683	128.8

Table 3.4: Mudstone depths, porosity, velocity, and vertical effective stress

Porosity is calculated from the log-derived travel time (sonic log) through Eq. 3.6. The average vertical effective stress for each sandstone is used to generate the dashed brown line in Fig. 3.13.

Sand	slope	y-intercept	R ²	$(\sigma_v - u_h) @ u^*_{sand} = u^*_{mudstone}$	
				PSI	MPA
N	1.14	-4533.4	0.98	5538	38.2
PQRS	0.88	-2870	0.74	5705	39.3
V	1.36	-6962	0.95	6575	45.3
DD, EE, FF	0.55	-177	0.77	6729	46.4

Table 3.5: Regression parameters ($u^* = a + b(\sigma_v - u_h)$) through the mudstone pressures at Mad Dog

The slope and y-intercept of the mudstone pressures are shown from Figure 3.13 (dashed black lines). The closer the slope is to 1.0 the more the mudstone pressures parallel the total vertical stress less the hydrostatic pressure (brown line, Figure 3.13). If the slope is less than 1.0, then the pore pressure is rising less than the total vertical stress. If the slope is greater than 1.0, then the pore pressure is rising more than the total stress. The total vertical stress less the hydrostatic pressure where the sandstone and mudstone excess pressures intersect are shown (projected intersections of dashed colored lines with dashed black line, Figure 3.13).

Appendix A: Estimation of Total Vertical Stress

The total vertical stress (σ_v) is calculated by integrating the bulk density with depth.

$$\sigma_v = \int \rho_{bulk} g dz \quad (\text{Eq. A.1})$$

The bulk density is taken from the wireline bulk density tool, but in zones where there is no wireline bulk density data, an empirical porosity and vertical effective stress relationship is used.

$$n = n_0 e^{-\beta(\sigma_v - u)} \quad (\text{Eq. A.2})$$

The pore pressure (u) is assumed to be hydrostatic by assuming a seawater density and sediment column water density of 1.023 g/cc (0.44 psi/ft).

The compressibility constant ($\beta = 3.68 \times 10^{-2} \text{ MPa}^{-1}$) and reference porosity ($n_0 = 0.40$) for mudstone were defined for a log-linear regression of n versus σ'_v (Hart et al., 1995).

Porosity calculated from equation A.2 is used to calculate the bulk density through equation A.3:

$$\rho_{bulk} = n \rho_f + (1 - n) \rho_{ma} \quad (\text{Eq. A.3})$$

where matrix density (ρ_{ma}) of 2.7 g/cc and a fluid density (ρ_f) of 1.075 g/cc were assumed.

The shallowest bulk density at Mad Dog was at 364 feet below the seafloor (FBSF) in well 826 #1, therefore the empirical relationship from equation A.2 was only used from the seafloor to 364 FBSF. The shallow bulk density section in well 826 #1 was used for other shallow sections at Mad Dog where no wireline bulk density was available. In zones where wells did not have a bulk density log (RHOB) offset wells were used to fill in the data (**Fig. A.1**).

In zones where salt is present at Mad Dog a constant bulk density of 2.2 g/cc was assumed (*Balk, 1949, 1953; Gera, 1972; Hudec et al., 2009; Lerche and Petersen, 1995; Nance et al., 1979; Nance and Wilcox, 1979*) (**Fig. A.2**). Others have used smaller salt densities at 2.076 g/cc at Walker Ridge 285 #1, 2.16 g/cc at Keathley Canyon, 2.165 g/cc for deepwater Gulf of Mexico seismic modeling (*Bird et al., 2005; Fredrich et al., 2007; Yarger et al., 2001*). Barker and Meeks (2003) noted that pure mineral halite has a density of 2.16 g/cc, but in the Gulf of Mexico in-situ salt density varies between 2.0-2.1 g/cc. Due to the viscous behavior at modest stresses and temperatures for salt, the density differences for can vary from 2.16 g/cc for pure halite (NaCl) or include other sediments at 2.3-2.6 g/cc (*Dusseault et al., 2004*).

Since the salt density at Mad Dog is unknown a density of 2.2 g/cc was assumed. If we assumed a salt density of 2.17 g/cc for wells 782 #1, 783 #1, and 826 #5 the total vertical stress would less. The difference in total vertical stress when using 2.2 g/cc vs. 2.17 g/cc results in a constant stress difference of 65 psi (0.45 MPa) for well 782 #1, 94 psi (0.65 MPa) for well 783 #1, and 35 psi (0.24 MPa) for well 826 #5. The thicker the salt is the larger affect the density of salt will have the total vertical stress below salt (i.e 783 #1 has the thickest salt, thus the higher difference between total vertical stress when changing salt densities). These are minimal changes in the total vertical stress regardless of which salt density is used.

A.1 FIGURES

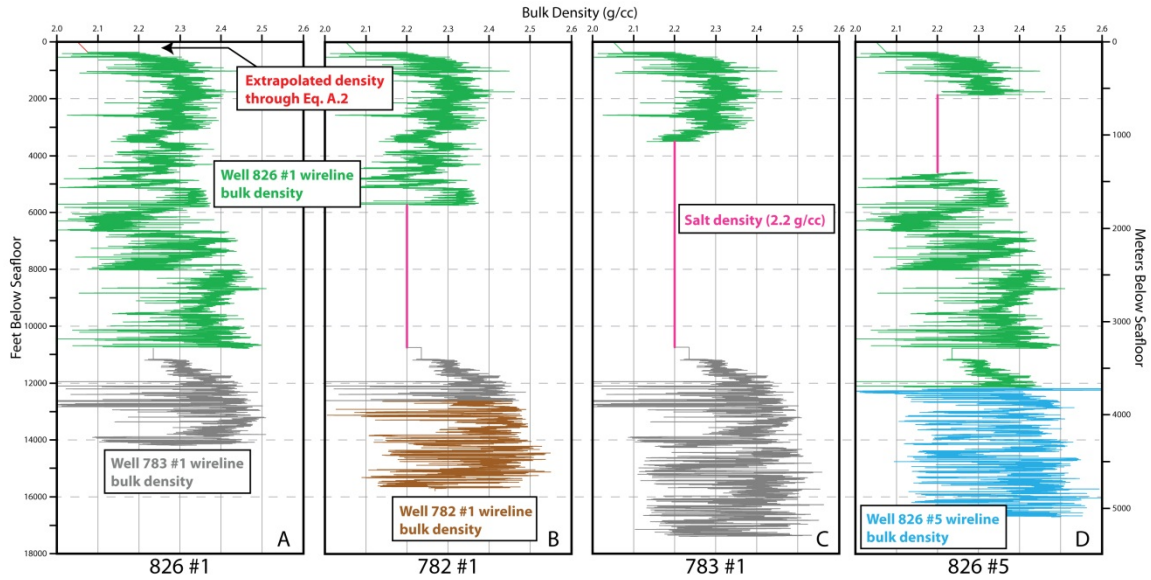


Figure A.1: Bulk densities for wells 826 #1, 782 #1, 783 #1, and 826 #5 used to calculate total vertical stress

(A) Well 826 #1 has an extrapolated bulk density from 0 to 364 feet below the seafloor (FBSF) through equation A.2. The wireline line bulk density was used from 364 feet below seafloor until 10777 FBSF and well 783 #1's wireline bulk density was used to total depth (TD). (B) Well 782 #1 has well 826 #1 bulk density from 0 to 5,747 FBSF to the top of salt. A salt density of 2.2 g/cc was assumed from 5,747 FBSF to 10,747 FBSF. From base of salt (10,747 FBSF) to 12,623 FBSF the wireline bulk density from the 783 #1 well was used and the wireline from 782 #1 was used until TD. (C) From 0 to the top of salt at 3,504 FBSF the wireline bulk density from well 826 #1 was used. A salt density of 2.2 g/cc was assumed from 3,504 to 10,739 FBSF. From the base of salt to TD the wireline bulk density was used from well 783 #1. (D) From 0 to the top of salt at 1,874 FBSF the wire bulk density from well 826 #1 was used. A salt density of 2.2 g/cc was assumed from 1,874 to 4,585 FBSF. From the base of salt to 12,183 FBSF the wireline bulk density from well 826 #1 was used and the rest of the well the wireline bulk density from well 826 #5 was used.

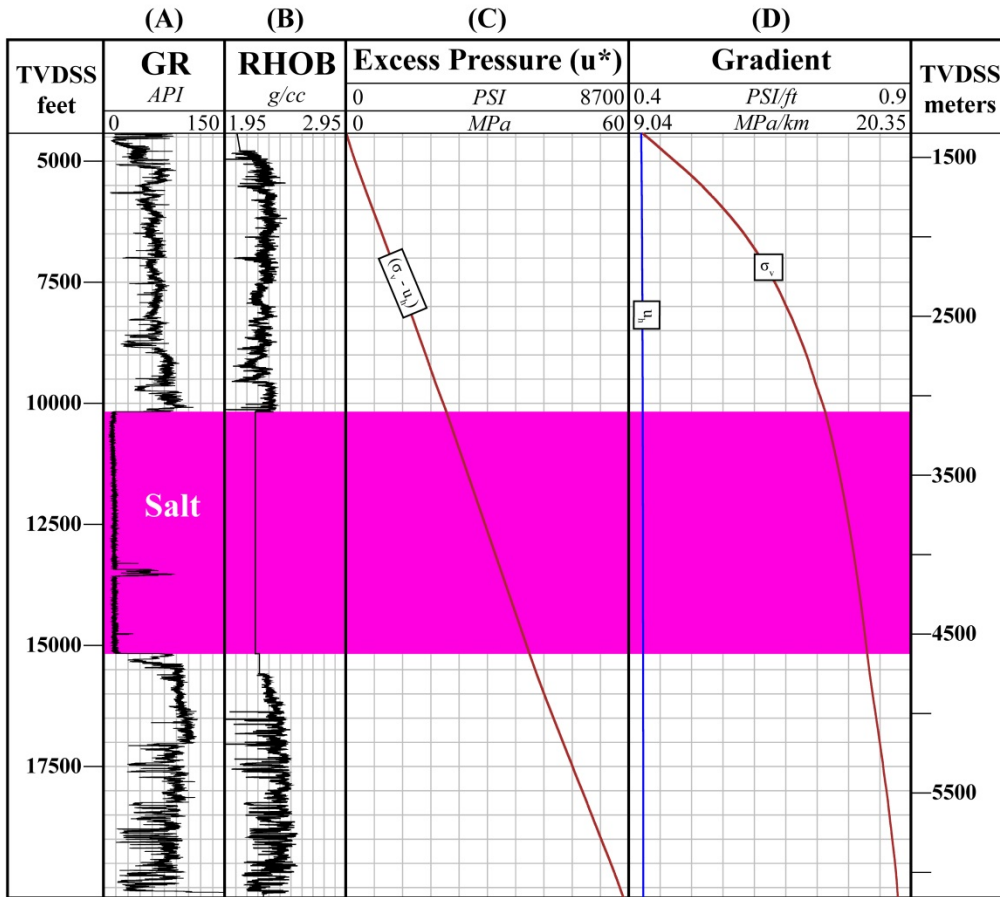


Figure A.2: Example calculation of the total vertical stress with salt present at Mad Dog from well 782 #1

The gamma ray log (A) and the bulk density log (B), where a constant bulk density of 2.2 g/cc was assumed where salt is present (Balk, 1949, 1953; Gera, 1972; Hudec et al., 2009; Lerche and Petersen, 1995; Nance et al., 1979; Nance and Wilcox, 1979). Above the salt the bulk density from well 826 #1 was assumed. The bulk density is integrated with depth from Eq. A.1 to produce the resulting total vertical stress (σ_v) curve and is plotted in excess pressure space (C). The excess pressure (u^*) was calculated by subtracting the absolute pressures/stresses from the integration of a constant water density of 1.023 g/cc (0.44 psi/ft) from the seafloor to the total depth. The gradient plot (D) was produced by dividing the hydrostatic pressure (u_h) and total vertical stress (σ_v) by TVDSS.

Appendix B: Methodology for Petrophysical Analysis

This appendix summarizes the steps used in chapter 3 to pick the mudstone intervals and filter the sonic log within a given well. The first section will describe how I used the wireline logs to manually pick the mudstone intervals. The last section will describe the steps used to develop a filtered sonic log in order to find the porosity. The discovery well 826 #1 is used in this appendix to demonstrate how to get the mudstone intervals and filtered sonic log.

The first step was determining the most accurate and reasonable way to pick the mudstone intervals within a given well. The less accurate and quicker approach to getting the mudstone intervals is taking the gamma ray curve, which is a lithology indicator and applying a filter throughout the entire well to determine the mudstone intervals. This technique was not reliable because of large variations in the gamma ray throughout the entire well and large variation in the resistivity and sonic logs where the mudstone intervals were picked. The large variations in the sonic log caused porosity and predicted pore pressure to be unrealistic.

The more accurate and reliable approach to determine the mudstone intervals was to first plot the gamma ray, resistivity, and sonic logs with depth (**Fig. B.1**). Next, the mudstone intervals are manually picked every 30 feet to 40 feet from the gamma ray log to get a good distribution of mudstone picks within a given well.

The resistivity and sonic logs are evaluated once the mudstone intervals are picked to make sure there are no skewed logs that do not agree with the mudstone picks. An example of a skewed log would be a large spike in the sonic log where the mudstone was picked. If the logs appear to be skewed where the mudstone was picked, the

mudstone pick is removed and not utilized. This technique was recommend through personal communication from Bowers (2012).

Once the mudstone intervals are picked the next step is to filter the sonic log. The first step is to take the sonic values where the mudstone intervals were manually picked. A smoothing average of 11 samples was used in order to eliminate noise from borehole effects or small lithology changes. In other words taking 11 samples means for a given point where the mudstone was picked, 5 points above and below are averaged where the mudstone interval was picked. This smoothing average helps to eliminate large spikes when the porosity and pore pressure is calculated. **Fig. B.1** illustrates the technique used to convert the original sonic log into a smoothed sonic log where the mudstone picks are.

B.1 FIGURES

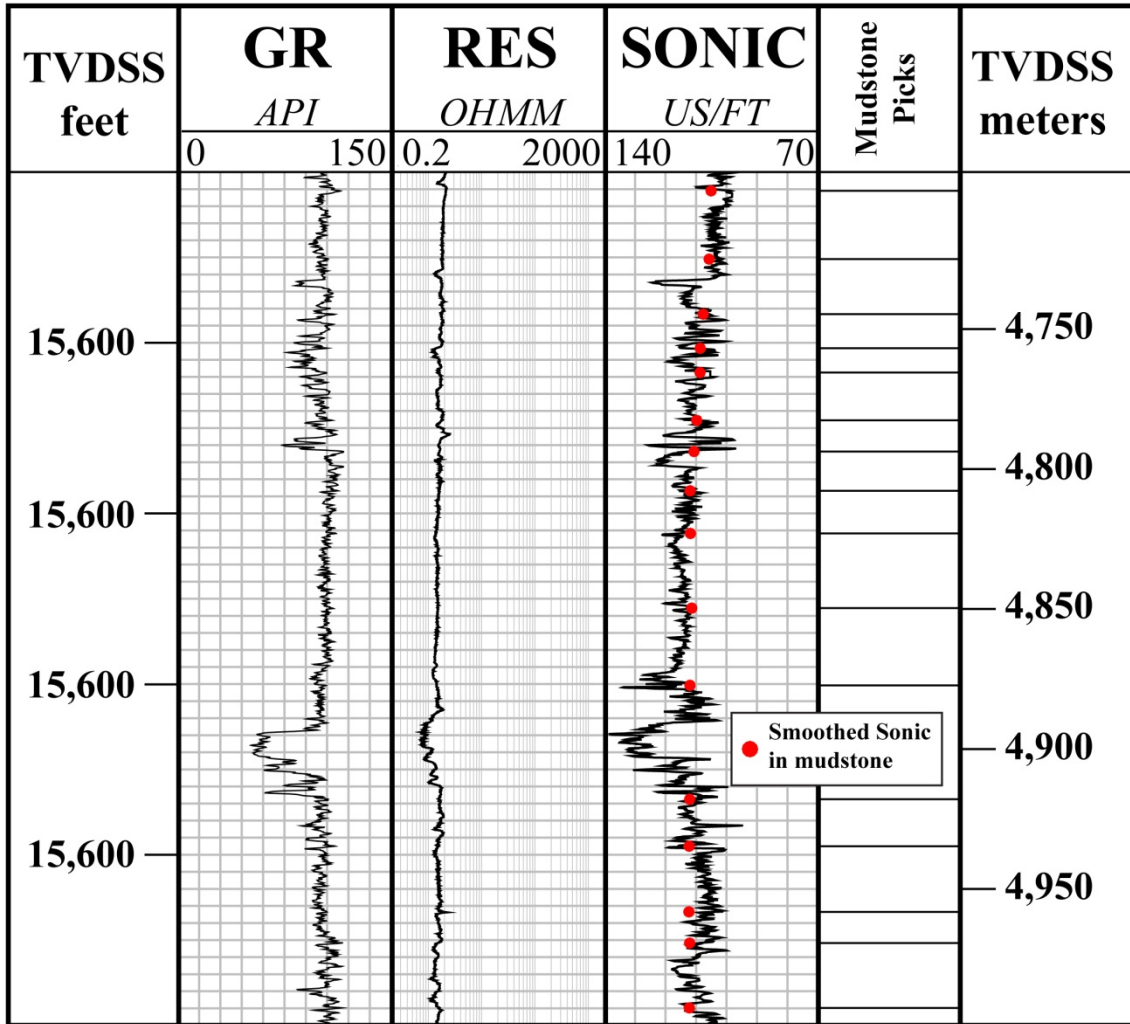


Figure B.1: Picking the mudstone intervals in well 826 #1

The mudstone intervals are manually picked every 30 feet to 40 feet using the gamma ray log. The resistivity and sonic logs are used to make sure there are no skewed values where the mudstone intervals are picked. If there are large spikes in the resistivity and sonic logs the mudstone intervals are removed. The solid lines in the mudstone picks log represent the manually picked mudstone intervals that are used for petrophysical analysis. The smooth mudstone sonic values (red circles) are calculated by taking a moving average of 11 samples (5 above and below).

Appendix C: Pore Pressure Prediction through Velocity

This appendix summarizes the technique used to calibrate a velocity and effective stress relationship at Mad Dog. The calibrated velocity and vertical effective stress relationship is then used to predict the mudstone pore pressure in several wells in the Mad Dog field. This technique is similar to the pressure prediction from porosity and vertical effective stress (Chapter 3) except that the velocity from the sonic log is used instead of converting the sonic log into porosity. This pore pressure prediction technique using the velocity and vertical effective stress is referred to as the Bowers Method (Bowers, 1995).

C.1 DEVELOPMENT OF A PREDICTIVE RELATIONSHIP

The velocity (v) and vertical effective stress (σ'_v) are related through an empirical relationship through equation C.1 (Bowers, 1995).

$$v = v_0 + A(\sigma'_v)^B \quad (\text{Eq. C.1})$$

Where v_0 is the seawater velocity, and A and B are empirical constants calibrated from velocity and vertical effective stress data. At Mad Dog a v_0 of 4930 ft/s was used. The vertical effective stress (σ'_v) is defined as the total vertical stress (σ_v) less the pore pressure (u) from equation C.2.

$$\sigma'_v = \sigma_v - u \quad (\text{Eq. C.2})$$

By combining equations C.1 and C.2 the fluid pressure can be predicted directly using equation C.3.

$$u = \sigma_v - \left(\frac{v-v_0}{A}\right)^{1/B} \quad (\text{Eq. C.3})$$

A velocity (v) and vertical effective stress (σ'_v) relationship on the shallow Pleistocene direct pore pressure measurements was achieved by the same steps used in chapter 3. Mudstone velocities are calculated from the sonic log in the following manner.

First, mudstone values were manually picked approximately every 30 feet (9 meters) to 40 feet (12 meters) based on the gamma ray log. A particular sonic velocity was chosen only if the gamma ray and resistivity log together indicated a mudstone interval. This removes the effect of high radioactive zones that are not characteristic mudstones. Where the mudstones were picked, a moving average of 11 samples was taken on the sonic log in order to smooth out the data to eliminate noise from borehole effects or small lithology changes. In other words, for each mudstone that was picked, 5 sonic log values from the picked mudstones above and below are averaged. The typical thickness of the averaging window is 400 feet (122 meters) on given mudstone pick.

The sonic log values were used to calculate the mudstone velocity through equation C.4

$$velocity (ft/s) = \frac{1}{Sonic\ Log\ \frac{us}{ft}} * (1 * 10^6) \quad (Eq. C.4)$$

Given velocity, we still need to know vertical effective stress to determine the A and B parameters in Eq. C.1. I know the total vertical stress within the mudstone (Appendix A, Eq. A.1) and must determine the pore pressure to determine vertical effective stress (Eq. C.2). My approach is to assume that the sandstone excess pressure equals the excess pressure within the nearest mudstone sample above and below.

The empirical constants A and B from equation C.1 were found by power regression on a plot of $(v-v_o)$ and effective stress (σ'_v) . The plot $(v-v_o)$ and effective stress (σ'_v) yields an A of 26.6 and a B of 0.63 (**Fig. C.1**). These constants through equation C.3 are used to predict the pore pressure in well 826 #1 (outboard of salt) and well 782 #1 (subsalt). These empirical constants of A and B are in agreements with another deepwater Gulf of Mexico study where $A = 28.3711$ and $B = 0.5207$ (Bowers, 1995).

The predicted pore pressures in well 826 #1 match the direct pressure measurements in the Pleistocene where we constrained the velocity and vertical effective stress relationship (**Fig. C.2**). In the shallow Pleistocene near the seafloor the predicted pore pressure shows a pressure increase, which matches shallow water flows documented from the drilling reports that indicate the presence of overpressure. From the Pleistocene to the upper Miocene the direct pressure measurements indicate a pore pressure increase and the predicted pore pressure matches this. The predicted pore pressure shows an increase from the middle to lower Miocene, similar to the direct pore pressure measurements but the predicted pore pressure slightly over predicts the direct pressure measurements. This behavior matches the predicted pressure from a porosity-vertical effective stress relationship in Chapter 3 (Fig. 3.4)

The predicted pore pressures in well 782 #1 (subsalt) predict a large excess pressure below salt in the upper Miocene and this matches the direct pore pressure measurements (**Fig. C.3**). Similar to the well 826 #1, the predicted pore pressure shows a pressure increase from the middle to lower Miocene and over predicts the direct pressure measurements. This behavior matches the predicted pressure from a porosity-vertical effective stress relationship in Chapter 3 (Fig. 3.5)

Whether I use the porosity-vertical effective stress (Chapter 3) or the velocity-vertical effective stress relationship to calibrate the relationship, the predicted pore pressures with depth are nearly identical. Therefore, either technique to predict pore pressure is valid.

C.2 FIGURES

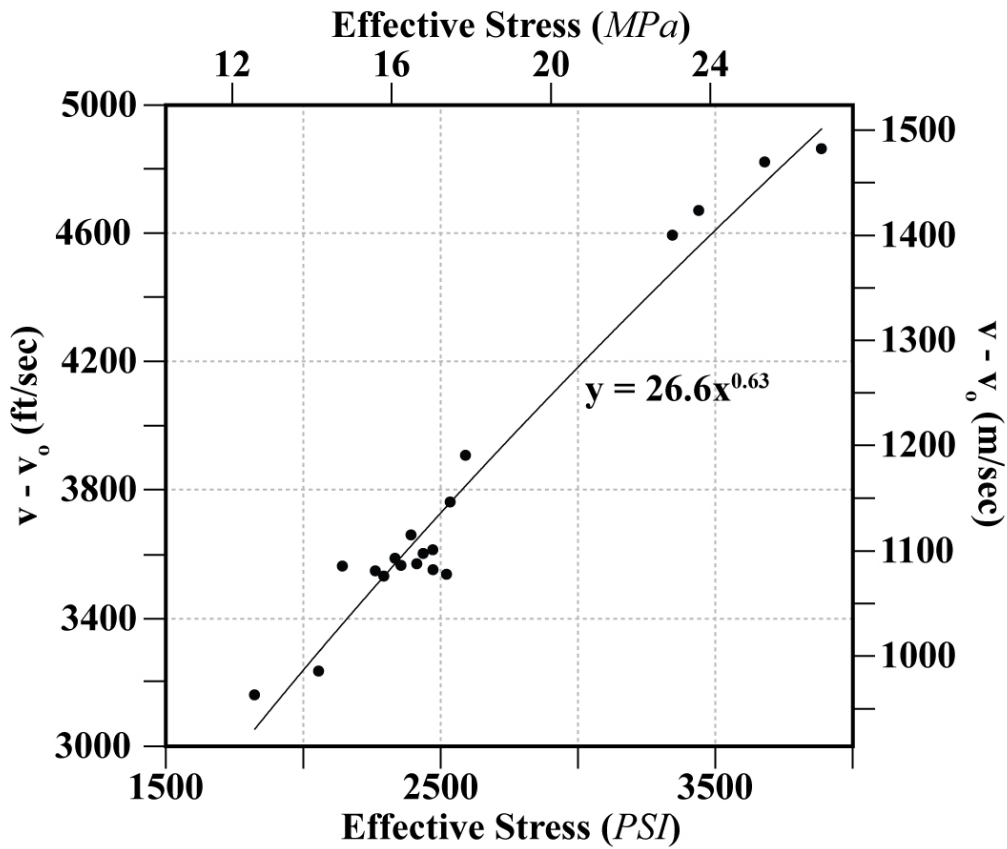


Figure C.1: Pleistocene mudstone velocity versus vertical effective stress in well 826 #1

The velocity and vertical effective stress relationship in the Pleistocene mudstones from the direct pressure measurements. The mudstone velocity and vertical effective stress relationship yielded an A of 26.6 and a B of 0.63.

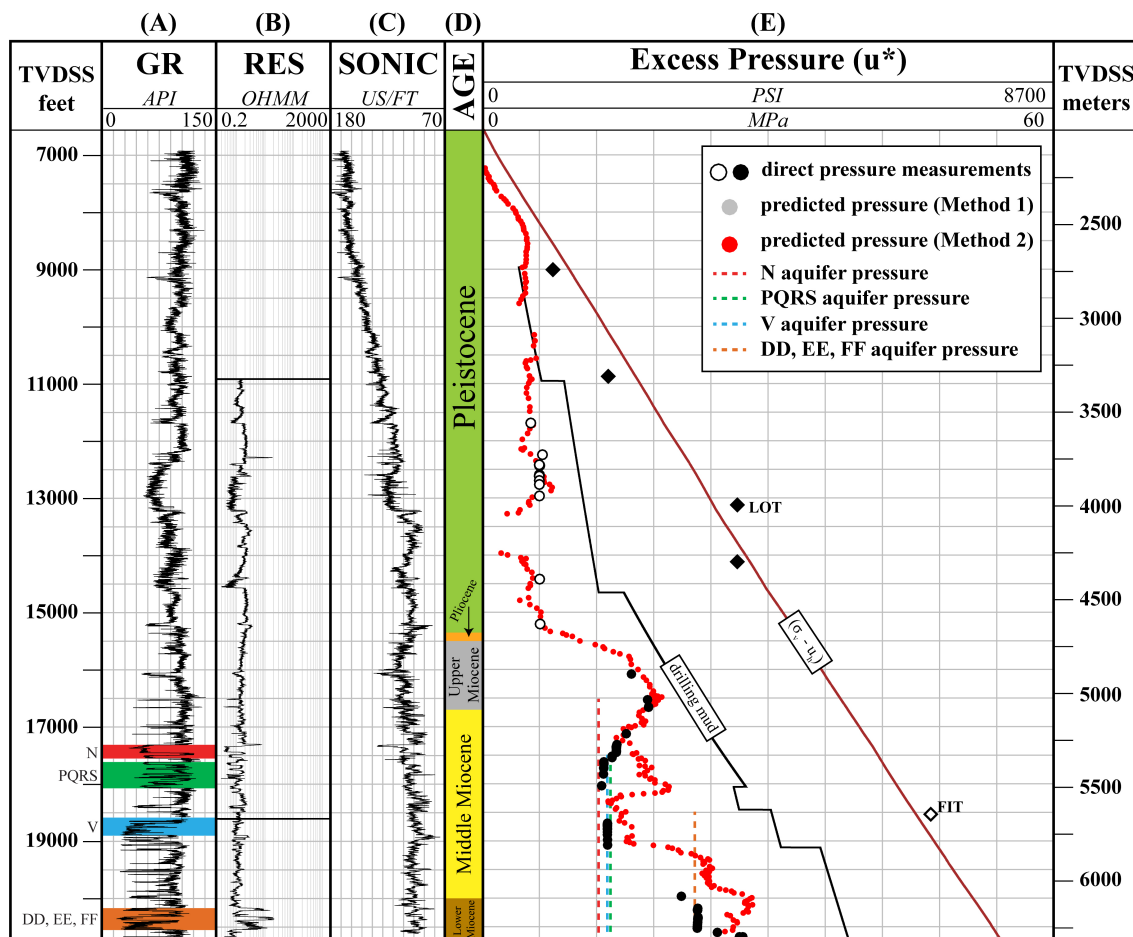


Figure C.2: Pressure versus depth plot of the discovery well 826 #1 using a velocity and vertical effective stress relationship to predict pressure

The wireline gamma ray, resistivity, and sonic logs (a-c) and the associated pressure and stress from the discovery well 826 #1 plotted in excess pressure (e) space. The predicted pore pressure (red circles) using the Pleistocene direct pressure measurements (open circles) for velocity-effective stress calibration provides an accurate pressure prediction in the Pleistocene and overestimates pressure in the Miocene. This prediction is nearly identical to the predicted using a porosity-effective stress relationship on Pleistocene direct pressure measurements (Fig. 3.4).

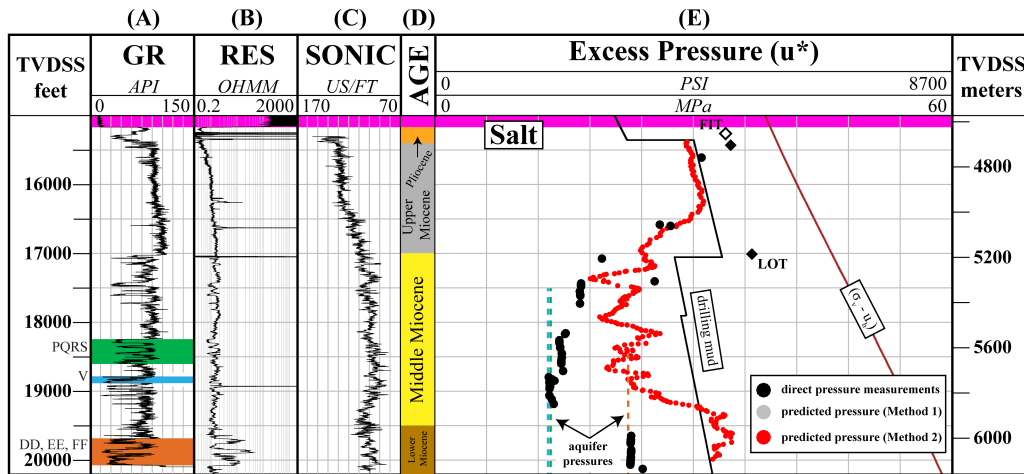


Figure C.3: Pressure versus depth plot of the first appraisal well 782 #1 using a velocity and vertical effective stress relationship to predict pressure

The wireline gamma ray, resistivity, and sonic logs (a-c) and the associated pressure and stress from the 1st appraisal well 782 #1 plotted in excess pressure (e) space. Well 782 #1 penetrated 5,000 feet (1,524 meters) of salt. The predicted pore pressure (red circles) matches direct pore pressure measurements (black circles) directly below salt except in the middle and lower Miocene where the prediction is overestimated. This prediction is nearly identical to the predicted using a porosity- effective stress relationship on Pleistocene direct pressure measurements (Fig. 3.5).

Appendix D: Shallow Pore Pressure Data

At Mad Dog there are several shallow sands above the main reservoir that have the presence of gas, oil, and water. This appendix summarizes the pressure distribution in the N, PQRS, and V sandstones across the Mad Dog field (Fig. D.1). These sands are interpreted as channel sandstones and are not as continuous as the DD, EE, and FF reservoir sandstone documented in Chapter 2 (Walker, 2012). Since these sandstones are more channel dominated the pressure data is more compartmentalized throughout the field, thus understanding the fluid distribution over large distances becomes challenging.

The N sandstone exhibits gas in the northeast and east regions of the field based on the resistivity log (Figs. 3.4b, 3.9b). In the north (well 783 #1) the gas gradient is 0.11 psi/ft (2.49 MPa/km) and in the east (well 826 #1) the gas gradient is 0.13 psi/ft (2.94 MPa/km) (Fig D.2). The gas phase pressure in the east is approximately 600 psi greater than the gas phase pressure in the northeast region, suggesting that the gas columns are not in pressure communication. The gas-water contact (GWC) in the northeast region was not penetrated, but the GWC was penetrated in the east region at 17,342 feet (5,286 meters) TVDSS with a water phase gradient of 0.45 psi/ft (10.18 MPa/km).

The PQRS sandstone lies directly below the N sandstone and is oil saturated in the northeast (well 783 #1) and east regions (well 826 #1) based on the resistivity log (Figs. 3.4b, 3.9b). The Mad Dog field is currently producing out of this sandstone in the northeast region from one well (well 783 #1). The sandstone exhibits two isolated oil phase pressures (Fig. D.3). The dominant oil gradient is 0.36 psi/ft (8.14 MPa/km) between both wells, but towards in the Upper PQRS sandstone in well 783 #1 the sandstone exhibits approximately 128 psi (0.88 MPa) higher oil phase pressure. The PQRS sandstone within well 782 #1 is water saturated based on the resistivity log (Fig.

3.5b). There are three isolated aquifers within this well that are on separate aquifer gradients between 0.42 psi/ft (9.5 MPa/km) and 0.45 psi/ft (10.18 MPa/km) and all of these are at higher pressures than the oil phase pressures in wells 782 #1 and 783 #1. Since the water phase pressure is larger than the oil phase pressure, these systems are not in pressure communication across the field. The OWC was not penetrated in the PQRS sandstone and the OWC cannot be projected because the water phase pressures are larger than the oil phase pressures.

The V sandstone lies directly below the PQRS sandstone and above the main reservoir sandstone (DD, EE, and FF). The V sandstone is water saturated throughout the field based on the resistivity curves (Figs. 3.4b, 3.5b, 3.9b, 3.10b). From the direct pressure measurements there are two separate pressure gradients. In wells 826 #1 and 783 #1 the pressures lie on the same water gradient of 0.43 psi/ft (9.73 MPa/km) with an overpressure of ≈ 1880 psi (12.96 MPa). In wells 782 #1 and 825 #6 the pressures lie on the same water gradient of 0.44 psi/ft (9.95 MPa/km) with an overpressure of ≈ 1932 psi (13.32 MPa).

D.1 FIGURES

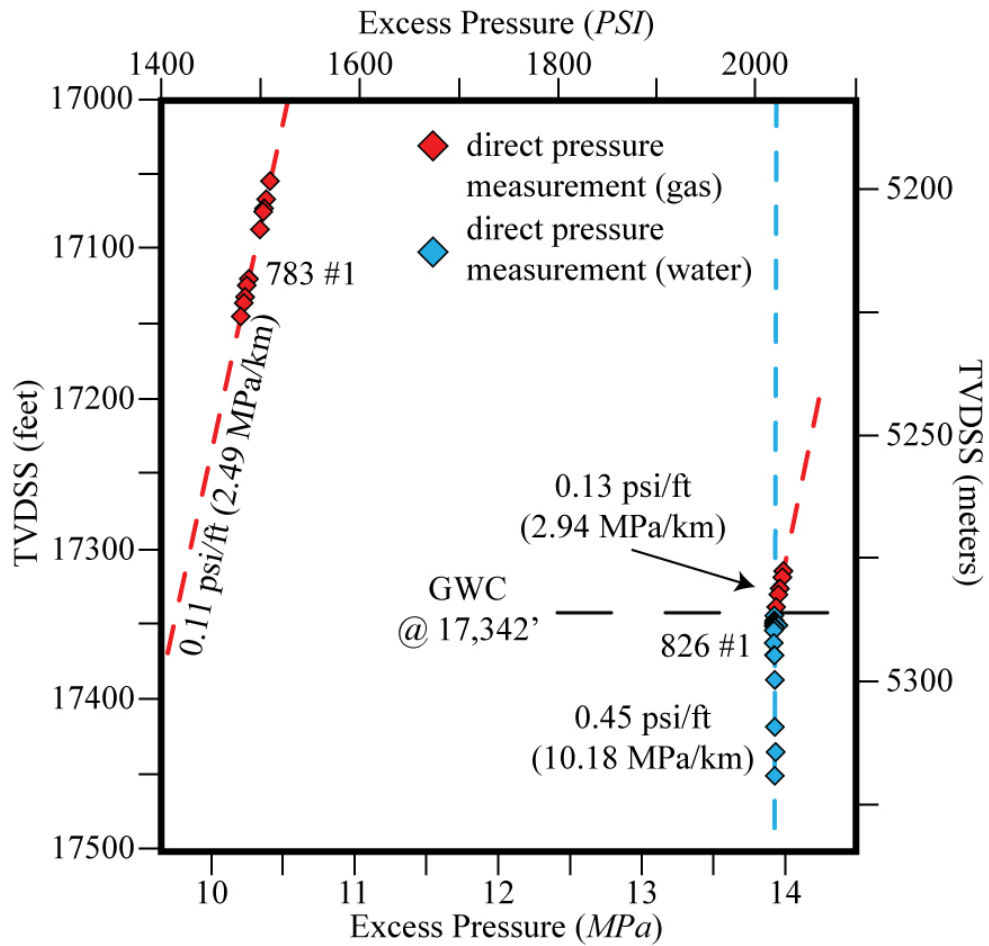


Figure D.1: Direct pressure measurements in the N sandstone

The north region of the Mad Dog field (well 783 #1) the gas gradient is 0.11 psi (2.49 psi/ft). In the east region of the Mad Dog field (well 826 #1) the gas-water contact was penetrated at 17,342 feet (5,286). The gas gradient was measured to be 0.13 psi/ft (2.94 MPa/km) and the water gradient measured 0.45 psi/ft (10.18 psi/ft). The N sandstone between well 783 #1 and 826 #1 are not in pressure communication due to the large pressure difference between the wells.

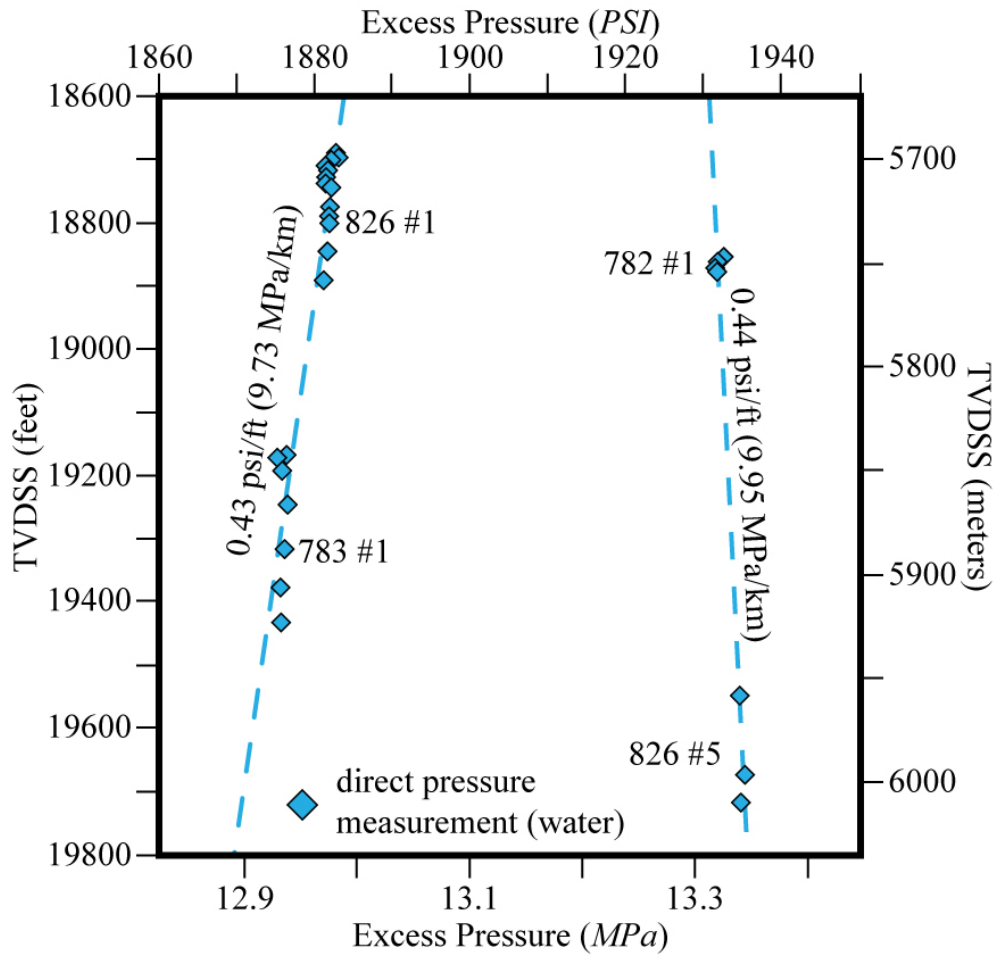


Figure D.3: Direct pressure measurements in the V sandstone

The V sandstone is water saturated throughout the Mad Dog field, therefore the direct pressure measurements measure the water phase pressure. Wells 783 #1 and 826 #1 lie on the same aquifer gradient of 0.43 psi/ft (9.73 MPa/km). Wells 782 #1 and 826 #5 lie on a different gradient of 0.44 psi/ft (9.95 MPa/km) and higher overpressure, suggesting the V is not in pressure communication across the field. Wells 783 #1 and 826 #1 are in pressure communication and well 782 #1 and 826 #5 are in pressure communication.

Appendix E: Depth below Seafloor versus Excess Pressure (u^*)

A common approach when looking at total vertical stress/ pore pressure plots is to plot them versus depth. In my case I plotted total vertical stress/pore pressure versus the total vertical stress less the hydrostatic pressure in Chapter 3 to look at the mudstone and sandstone pressures. I utilized this approach in Chapter 3 because the regression taken through the mudstone pressures provided a better match (R^2 approaching 1.0). The excess pressures (u^*) versus the depth below the seafloor are shown for all 4 main reservoir sandstones (Figure E.1) and a summary of the regression parameters is shown in (Table E.1).

E.1 FIGURES

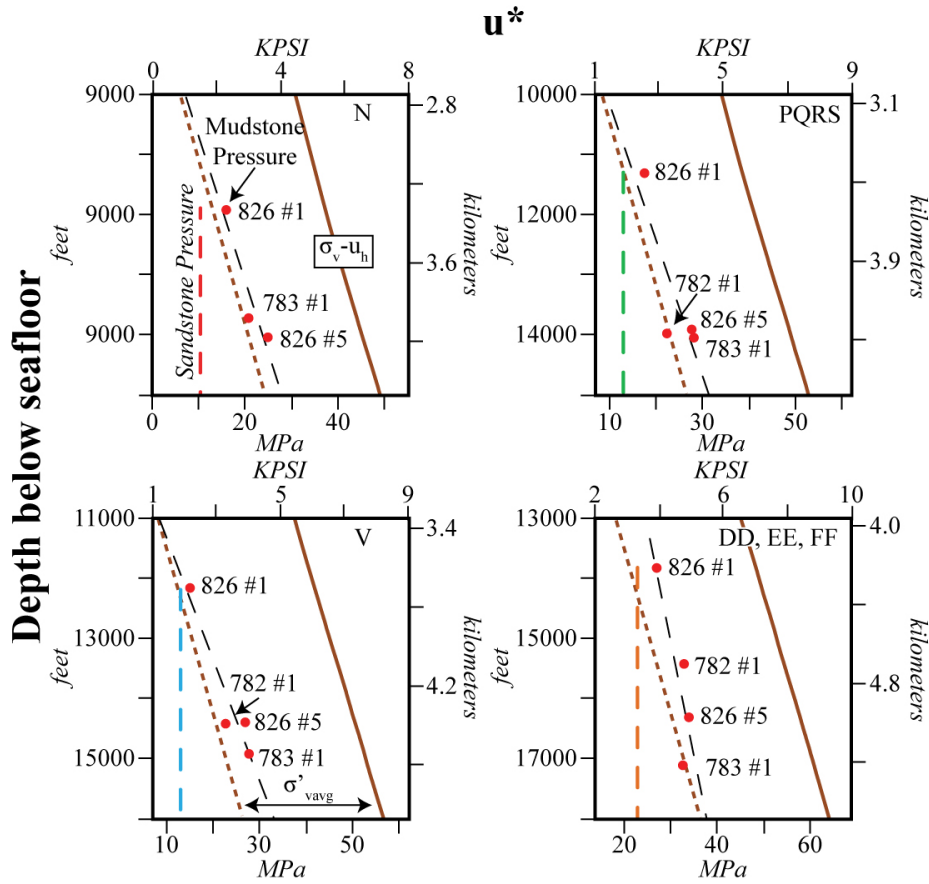


Figure E.1: Sandstone and mudstone pressures across the field (depth below seafloor versus excess pressure)

The depth below the seafloor plotted against excess pressure (u^*). The sandstone excess pressures (black lines) appear as a vertical line and the mudstone excess pressures (red circles) increase with increasing depth. A regression is taken through the mudstone excess pressures (dashed black line) and this line more or less parallels the $\sigma_v - u_h$ curve (brown line). The brown dashed line, drawn parallel to the $\sigma_v - u_h$ curve (solid brown line) shows an alternative fit of the data, in which $u^* = (\sigma_v - u_h) - \sigma'_{vavg}$, and σ'_{vavg} is the average vertical effective stress for each group (Table 3.4). The sandstone excess pressures are extrapolated to the shallowest penetration at Mad Dog. Table E.1 summarizes the slope, y-intercept, R^2 , and $\sigma_v - u_h$ at the projected intersection of the sandstone and mudstone excess pressures.

E.2 TABLES

Sand	slope	y-intercept	R ²	$(\sigma_v - u_h) @ u^*_{sand} = u^*_{mudstone}$	
				PSI	MPA
N	0.53	-3571	0.89	10212	70.4
PQRS	0.46	-2691	0.72	31351	216.2
V	0.65	-5724	0.91	11965	82.5
DD, EE, FF	0.27	316	0.71	12184	84.0

Table E.1: Regression parameters ($u^* = a + b(\sigma_v - u_h)$) through the mudstone pressures at Mad Dog using depth

The slope and y-intercept of the mudstone pressures are shown from Figure E.1 (dashed black lines). The closer the slope is to 1.0 the more the mudstone pressures parallel the total vertical stress less the hydrostatic pressure (brown line, Figure 3.13). If the slope is less than 1.0, then the pore pressure is rising less than the total vertical stress. If the slope is greater than 1.0, then the pore pressure is rising more than the total stress. The total vertical stress less the hydrostatic pressure where the sandstone and mudstone excess pressures intersect are shown (projected intersections of dashed colored lines with dashed black line, Figure E.1). Note that the R² values between Table 3.5 and the table above show that the regression parameters in Table 3.5 are better (R² closer to 1.0).

Bibliography

- Aharon, P., H. H. Roberts, and R. Snelling, 1992, Submarine venting of brines in the deep Gulf of Mexico: Observations and geochemistry: *Geology*, v. 20, p. 483-486.
- Athy, L. F., 1930, Density, Porosity, and Compaction of Sedimentary Rocks: *American Association of Petroleum Geologists*, v. 14, p. 1-22.
- Badri, M. A., C. Sayers, R. A. Hussein, and A. Graziano, 2001, Pore pressure prediction data using seismic velocities and log data in the Offshore Nile Delta, Egypt, SPE Middle East Oil Show, Bahrain, Society of Petroleum Engineers Inc.
- Balk, R., 1949, Structure of grand saline salt dome, Van Zandt County, Texas: *AAPG Bulletin*, v. 33, p. 1791-1829.
- Balk, R., 1953, Salt structure of Jefferson Island salt dome, Iberia and Vermilion Parishes, Louisiana: *AAPG Bulletin*, v. 37, p. 2455-2474.
- Barker, J. W., and W. R. Meeks, 2003, Estimating fracture gradient in Gulf of Mexico deepwater, shallow, massive salt sections, SPE Annual Technical Conference and Exhibition, Denver, Colorado, Society of Petroleum Engineers.
- Bird, D. E., K. Burke, S. A. Hall, and J. F. Casey, 2005, Gulf of Mexico tectonic history: hotspot tracks, crustal boundaries, and early salt distribution: *AAPG Bulletin*, v. 89, p. 311-328.
- Bowers, G., 2012, Personal communication, Houston.
- Bowers, G. L., 1995, Pore pressure estimation from velocity data: accounting for overpressure mechanisms besides undercompaction: *SPE Drilling & Completion*, p. 89-95.
- Bowers, G. L., 2007, Effect of inelastic sediment behavior on near-salt stresses and pore pressures: *The Leading Edge*, v. 26, p. 1462-1465.
- Bredehoeft, J. D., and B. B. Hanshaw, 1968, On the maintenance of anomalous fluid pressures: I. thick sedimentary sequences: *Geological Society of America Bulletin*, v. 79, p. 1097-1106.
- Carcione, J. M., and H. B. Helle, 2002, Rock physics of geopressure and prediction of abnormal pore fluid pressure using seismic data: *Canadian Society of Exploration Geophysicists*, v. 27, p. 8-32.
- Dias, T. A., D. L. Tett, and M. T. Croasdaile, 2009, Evidence for a hydrodynamic aquifer in the Lower Miocene sands of the Mad Dog Field, Gulf of Mexico, AAPG Convention, Denver, Colorado, p. 1-9.
- Dusseault, M. B., V. Maury, F. Sanfilippo, and F. J. Santarelli, 2004, Drilling through salt: constitutive behavior and drilling strategies, *American Rock Mechanics Association*.
- Ebrom, D., P. Heppard, and M. Albertin, 2006, Travel-time methods of vp/vs determination for pore-pressure prediction using look-ahead vsps, *Offshore Technology Conference*, Houston, Texas.
- Fertl, W. H., R. E. Chapman, and R. F. Hotz, 1994, *Studies in abnormal pressures*, Elsevier.

- Flemings, P. B., and J. A. Lupa, 2004, Pressure prediction in the Bullwinkle basin through petrophysics and flow modeling (Green Canyon 65, Gulf of Mexico): *Marine and Petroleum Geology*, v. 21, p. 1311-1322.
- Flemings, P. B., B. B. Stump, T. Finkbeiner, and M. Zoback, 2002, Flow focusing in overpressured sandstones: Theory, observations, and applications: *American Journal of Science*, v. 302, p. 827-855.
- Fredrich, J. T., D. Coblenz, A. F. Fossum, and B. J. Thorne, 2003, Stress perturbations adjacent to salt bodies in the deepwater Gulf of Mexico, SPE Annual Technical Conference and Exhibition, Denver, Colorado, Society of Petroleum Engineers.
- Fredrich, J. T., B. P. Engler, J. A. Smith, E. C. Onyia, and D. Tolman, 2007, Predrill estimation of subsalt fracture gradient: analysis of the Spa prospect to validate nonlinear finite element stress analyses, SPE/IADC Drilling Conference, Amsterdam, The Netherlands, p. 1-8.
- French, F. R., and M. R. McLean, 1993, Development drilling problems in high-pressure reservoirs: *SPE Journal of Petroleum Technology*, v. 45, p. 772-777.
- Gealy, B. L., 1955, Topography of the continental slope in northwest Gulf of Mexico: *Bulletin of the Geological Society of America*, v. 66, p. 203-228.
- Gera, F., 1972, Review of salt tectonics in relation to the disposal of radioactive wastes in salt formations: *Geological Society of America Bulletin*, v. 83, p. 3551-3574.
- Gismatullin, E., 2011, BP doubles oil estimate from Gulf of Mexico's Mad Dog Field, www.bloomberg.com.
- Harrison, W. J., and L. L. Summa, 1991, Paleohydrology of the Gulf of Mexico basin: *American Journal of Science*, v. 291, p. 109-176.
- Hart, B. S., P. B. Flemings, and A. Deshpande, 1995, Porosity and pressure: role of compaction disequilibrium in the development of geopressures in a Gulf Coast Pleistocene basin: *Geology*, v. 23, p. 45-48.
- Hudec, M. R., M. P. A. Jackson, and D. D. Schultz-Ela, 2009, The paradox of minibasin subsidence into salt: clues to the evolution of crustal basins: *Geological Society of America Bulletin*, v. 121, p. 201-221.
- Issler, D. R., 1992, A new approach to shale compaction and stratigraphic restoration, Beaufort-Mackenzie basin and Mackenzie corridor, northern Canada: *American Association of Petroleum Geologists Bulletin*, v. 76, p. 1170-1189.
- Kim, C. M., 1988, Field measurement of borehole closure across salt formation: implementation to well cementing, SPE Annual Technical Conference and Exhibition, Houston, Texas, Society of Petroleum Engineers, p. 1-4.
- Lerche, I., and K. Petersen, 1995, *Salt and sediment dynamics*, Taylor & Francis.
- Luo, G., M. A. Nikolinakou, P. B. Flemings, and M. R. Hudec, 2012a, Geomechanical modeling of stresses adjacent to salt bodies: part 1—uncoupled models: *AAPG Bulletin*, v. 96, p. 43-64.
- Luo, G., M. A. Nikolinakou, P. B. Flemings, and M. R. Hudec, 2012b, Near-salt stress and wellbore stability: A finite-element study and its application, *American Rock Mechanics Association*, Chicago, IL, p. 1-9.

- Michell, S., J. Sharp, and D. Chergotis, 2007, Dual-azimuth versus wide-azimuth technology as applied in subsalt imaging of Mad Dog Field—a case study: *The Leading Edge*, v. 26, p. 470-478.
- Moore, M. G., G. M. Apps, and F. J. Peel, 2001, The petroleum system of the western Atwater Foldbelt in the ultra deep water Gulf of Mexico, GCSSEPM Foundation 21st Annual Research Conference, p. 369-380.
- Mukerji, T., N. Dutta, M. Prasad, and J. Dvorkin, 2002, Seismic detection and estimation of overpressures part 1: the rock physics basis: *Canadian Society of Exploration Geophysicists*, v. 27, p. 34-57.
- Nance, D., J. Rovik, and R. E. Wilcox, 1979, Lithology of the vacherie salt dome core: a topical report, Louisiana State University, Institute for Environmental Studies, 343 p.
- Nance, D., and R. E. Wilcox, 1979, Lithology of the rayburn's dome salt core: a topical report, Louisiana State University, Institute for Environmental Studies, 307 p.
- Nikolinakou, M. A., G. Luo, M. R. Hudec, and P. B. Flemings, 2011, Geomechanical modeling of stresses and pore pressures In mudstones adjacent to salt bodies, *American Rock Mechanics Association*, p. 1-8.
- Nikolinakou, M. A., G. Luo, M. R. Hudec, and P. B. Flemings, 2012, Geomechanical modeling of stresses adjacent to salt bodies: part 2—Poroelastoplasticity and coupled overpressures: *AAPG Bulletin*, v. 96, p. 65-85.
- Orange, D. L., M. M. Angell, J. R. Brand, J. Thomson, T. Buddin, M. Williams, W. Hart, and W. J. B. III, 2003, Geological and shallow salt tectonic setting of the Mad Dog and Atlantis fields: relationship between salt, faults, and seafloor geomorphology, *Offshore Technology Conference*, Houston, Texas, p. 1-16.
- Raymer, D. G., A. Tommasi, and J.-M. Kendall, 2000, Predicting the seismic implications of salt anisotropy using numerical simulations of halite deformation: *Geophysics*, v. 65, p. 1272-1280.
- Rohleder, S. A., W. W. Sanders, R. N. Williamson, G. L. Faul, and L. B. Dooley, 2003, Challenges of drilling an ultra-deep well in deepwater - Spa prospect, *Society of Petroleum Engineers International Association of Drilling Contractors Drilling Conference*, Amsterdam, Netherlands, SPE/IADC Drilling Conference, p. 1-15.
- Rubey, W. W., and M. K. Hubbert, 1959, Role of fluid pressure in mechanics of overthrust faulting: *Geological Society of America Bulletin*, v. 70, p. 115-166.
- Sanford, J., J. Woomer, J. Miller, and C. Russell, 2006, The K2 project: a drilling engineer's perspective, *Offshore Technology Conference*, Houston, Texas, p. 1-11.
- Sayers, C. M., G. M. Johnson, and G. Denyer, 2002, Predrill pore-pressure prediction using seismic data: *Geophysics*, v. 67, p. 1286-1292.
- Seldon, B., and P. B. Flemings, 2005, Reservoir pressure and seafloor venting: predicting trap integrity in a Gulf of Mexico deepwater turbidite minibasin: *AAPG Bulletin*, v. 89, p. 193-209.
- Sharp, J. M., and P. A. Domenico, 1976, Energy transport in thick sequences of compacting sediment: *Geological Society of America Bulletin*, v. 87, p. 390-400.

- Smith, T., D. Kenney, M. Dimarco, M. Poulin, A. Trevena, and G. Steffens, 2001, Geological and geophysical reservoir description at Mad Dog Field—An ultra-deepwater, sub-salt oil discovery in the Gulf of Mexico (abstract), Unocal Technology Conference, Bangkok, Thailand.
- Sweatman, R., R. Faul, and C. Ballew, 1999, New solutions for subsalt-well lost circulation and optimized primary cementing, SPE Annual Technical Conference and Exhibition, Houston, Texas, Society of Petroleum Engineers, p. 1-11.
- Sweet, M. L., and L. T. Sumpter, 2007, Genesis field, Gulf of Mexico: recognizing reservoir compartments on geologic and production time scales in deep-water reservoirs: AAPG Bulletin, v. 91, p. 1701-1729.
- Viceer, S., M. L. Albertin, G. Vinson, B. Hornby, D. Ebrom, P. Heppard, C. Jay, and J.-P. Blangy, 2006, Improving drilling efficiency using a look-ahead vsp to predict pressure, exiting salt: five Gulf of Mexico examples, Offshore Technology Conference, Houston, Texas, p. 1-4.
- Walker, C., 2012, Personal communication, Houston.
- Walker, C., P. Belvedere, J. Petersen, S. Warrior, A. Cunningham, G. Clemenceau, C. Huenink, and R. Meltz, 2012, Straining at the leash: understanding the full potential of the deep-water, sub-salt Mad Dog field, from appraisal through early production, 32nd Annual GCSSEPM Foundation Bob F. Perkins Research Conference, New Understanding of the Petroleum Systems of Continental Margins of the World, p. 1-37.
- Weatherl, M. H., 2010, GOM deepwater field development challenges at Green Canyon 468 Pony, SPE Deepwater Drilling and Completions Conference, Galveston, Texas, USA, Society of Petroleum Engineers, p. 1-15.
- Whitson, C. D., and M. K. McFadyen, 2001, Lessons learned in the planning and drilling of deep, subsalt wells in the deepwater Gulf of Mexico, SPE Annual Technical Conference and Exhibition, New Orleans, Louisiana, Society of Petroleum Engineers Inc., p. 1-9.
- Williams, K. E., R. Redhead, and W. Standifird, 2008, Geopressure analysis in the subsalt Knotty Head field: deepwater Gulf of Mexico, Gulf Coast Association of Geological Societies Transactions, p. 905-912.
- Willson, S. M., and J. T. Fredrich, 2005, Geomechanics considerations for through- and near-salt well design, SPE Annual Technical Conference and Exhibition, Dallas, Texas, Society of Petroleum Engineers, p. 1-17.
- Yarger, H., L. DeKay, and E. G. Hensel, 2001, Salt canopy modeling with gravity in deepwater Gulf of Mexico.